

AN EXTRAGALACTIC ¹²CO $J = 3-2$ SURVEY WITH THE HEINRICH-HERTZ-TELESCOPE

RUI-QING MAO^{1,2}, ANDREAS SCHULZ^{3,4}, CHRISTIAN HENKEL², RAINER MAUERSBERGER⁵, DIRK MUDERS² AND
DIHN-V-TRUNG^{6,7}

Accepted for publication in The Astrophysical Journal

ABSTRACT

We present results of a ¹²CO $J = 3-2$ survey of 125 nearby galaxies obtained with the 10-m Heinrich-Hertz-Telescope, with the aim to characterize the properties of warm and dense molecular gas in a large variety of environments. With an angular resolution of 22'', ¹²CO 3-2 emission was detected in 114 targets. Based on 61 galaxies observed with equal beam sizes the ¹²CO 3-2/1-0 integrated line intensity ratio R_{31} is found to vary from 0.2 to 1.9, with an average value of 0.81. No correlations are found for R_{31} to Hubble type and far infrared luminosity. Possible indications for a correlation with inclination angle and the 60 μ m/100 μ m color temperature of the dust are not significant. Higher R_{31} ratios than in “normal” galaxies, hinting at enhanced molecular excitation, may be found in galaxies hosting active galactic nuclei. Even higher average values are determined for galaxies with bars or starbursts, the latter being identified by the ratio of infrared luminosity versus isophotal area, $\log [(L_{\text{FIR}}/L_{\odot})/(D_{25}^2/\text{kpc}^2)] > 7.25$. (U)LIRGs are found to have the highest averaged R_{31} value. This may be a consequence of particularly vigorous star formation activity, triggered by galaxy interaction and merger events. The nuclear CO luminosities are slightly sublinearly correlated with the global FIR luminosity in both the ¹²CO $J = 3-2$ and the 1-0 lines. The slope of the log-log plots rises with compactness of the respective galaxy subsample, indicating a higher average density and a larger fraction of thermalized gas in distant luminous galaxies. While linear or sublinear correlations for the ¹²CO $J = 3-2$ line can be explained, if the bulk of the observed $J = 3-2$ emission originates from molecular gas with densities below the critical one, the case of the ¹²CO $J = 1-0$ line with its small critical density remains a puzzle.

Subject headings: galaxies: ISM – galaxies: starburst – galaxies: active – radio lines: galaxies – ISM: molecules – surveys

1. INTRODUCTION

Low lying rotational transitions of CO are widely used as tracers of molecular hydrogen and are essential to determine dynamical properties and total molecular masses of galaxies. The widespread use of ¹²CO $J = 1-0$ and 2-1 (hereafter CO(1-0) and CO(2-1)) spectroscopy (e.g. Braine et al. 1993; Young et al. 1995; Chini et al. 1996; Elfhag et al. 1996; Albrecht et al. 2004, 2007) is, however, not sufficiently complemented by systematic surveys in higher rotational CO transitions to constrain the excitation conditions of the dense interstellar medium (ISM). While the $J = 1$ and 2 states of CO are only 5.5 and 17K above the ground level, the $J = 3$ state is at 33K and traces a component of higher excitation. The “critical densities”, at which collisional de-excitation matches spontaneous decay in the optically thin limit, is $\sim 10^5 \text{ cm}^{-3}$ for ¹²CO $J = 3-2$ (hereafter CO(3-2)) in

contrast to $10^{3.5}$ and $10^{4.3} \text{ cm}^{-3}$ for the two lower rotational CO transitions. Therefore, the CO(3-2) line is a particularly useful tracer of the molecular gas properties in the central regions of galaxies, where the molecular gas is generally believed to be warmer and denser than in typical galactic disk clouds (e.g., Güsten et al. 1981; Mauersberger & Henkel 1993). The CO(3-2) to (1-0) line intensity ratio is better suited to constrain the gas temperature and density than the ratio of CO(2-1) to (1-0).

In the local universe, most of the evidence for a higher excited gas phase comes from species other than CO. In many cases, however, such rare molecular species are difficult to detect, particularly in higher excited transitions. To investigate properties (e.g. spatial density, column density, kinetic temperature) of the bulk of the gas for a large sample of galaxies, observations of strong lines are needed. Thus, CO transitions of higher excitation have to be observed. This has been proved to be very successful in the first extragalactic CO(3-2) survey encompassing a significant (29) number of galaxies (Mauersberger et al. 1999), in which CO(3-2) was detected in all of the targets studied.

Encouraged by this result (see also Devereux et al. 1994), we have used the Heinrich Hertz Telescope (HHT) on Mt. Graham (Baars & Martin 1996) to observe the CO(3-2) line in an extended sample of galaxies. After we started this extended project, additional extragalactic CO(3-2) surveys have been carried out, aiming at different types of galaxies. These include Virgo cluster galax-

¹ Purple Mountain Observatory, Chinese Academy of Sciences, 210008 Nanjing, PR China; rqqmiao@pmo.ac.cn

² Max-Planck-Institut für Radioastronomie, Auf dem Hügel 69, D-53121 Bonn, Germany

³ Argelander-Institut für Astronomie, Universität Bonn, Auf dem Hügel 71, D-53121 Bonn, Germany

⁴ Institut für Physik und ihre Didaktik, Universität zu Köln, Gronewaldstr. 22, D-50931 Köln, Germany

⁵ Joint ALMA Observatory, Av. Alonso de Córdova 3107, Vitacura, Santiago, Chile

⁶ Institute of Astronomy and Astrophysics, Academia Sinica, Taipei, Taiwan

⁷ Center for Quantum Electronics, Institute of Physics, Vietnamese Academy of Science and Technology, 10 DaoTan, BaDinh, Hanoi, Vietnam

ies (Hafok & Stutzki 2003), infrared luminous galaxies (Yao et al. 2003; Narayanan et al. 2005), early type galaxies (Vila-Vilaró et al. 2003), compact and dwarf galaxies (Meier et al. 2001; Israel 2005), double barred galaxies (Petitpas & Wilson 2003, 2004), nearby galaxies of various types (Bayet et al. 2006), and most recently some nearby spiral and elliptical galaxies with two newly mounted submillimeter telescopes in Chile, APEX and ASTE (Nakanishi et al. 2007; Komugi et al. 2007; Galaz et al. 2008). Some extended CO(3–2) maps were also reported toward a handful of nearby galaxies (e.g., Dumke et al. 2001; Muraoka et al. 2009; Warren et al. 2010). Interferometric CO(3–2) maps of individual galaxies are also feasible thanks to the Submillimeter Array (hereafter SMA; see, e.g., Wilson et al. 2008, 2009). However, the detailed study of warm gas in nearby galaxies is still in its infancy. This is regrettable, in particular because of its crucial role in highly redshifted targets, where not CO(1–0) but higher excited CO lines are commonly observed (e.g., Solomon & Vanden Bout 2005).

In this paper, we present the results of our survey, which covers the by far largest sample of galaxies measured so far in the CO(3–2) line. The data were obtained in a “coherent” way, making use of a specific telescope/receiver/backend combination. With complementary information from CO(1–0), taken from the literature, we thus present a data base of unprecedented size, providing a suitable basis to check the quality of our data (as well as those reported earlier) and allowing us to tackle a number of astrophysical questions. The data are used for the following main purposes: 1) to provide a large and homogeneous data set of CO(3–2) spectra, which will form an essential basis for future studies, either aiming at higher angular resolution or searching for higher excited CO transitions see, e.g., (Van der Werf et al. 2010) for a pioneering study), 2) to systematically trace the global properties of the warm and dense molecular gas in various galaxies, 3) to test whether there are any correlations between the molecular gas excitation (given by the CO(3–2)/CO(1–0) intensity ratio) and galaxy properties such as Hubble type, nuclear activity, far infrared (FIR:40–400 μm) luminosity, 60 μm /100 μm color temperature of the dust, and inclination, 4) to evaluate the effect of galaxy interactions on the molecular gas properties, 5) to test whether the CO(3–2) line is a better tracer of star formation than the CO(1–0) line, and 6) to evaluate the Schmidt-Kennicutt law in the light of the new data. We present the sample selection in §2, the observations in §3, the basic results in §4, a systematic analysis of correlations in §5, and the summary in §6.

2. THE SAMPLES

2.1. Sample selection

Our sample selected for the CO(3–2) survey consists of 125 galaxies which are part of five major partially overlapping sub-samples. Table 1 lists all the sample galaxies along with some basic properties mostly drawn from the

NED⁸ and HyperLEDA⁹ (Paturel et al. 2003).

The first sub-sample consists of 58 nearby galaxies of various types. It contains 22 reobserved sources that were already part of our initial survey (Mauersberger et al. 1999), and is complemented by the remaining IRAS point sources with $S_{100\mu\text{m}} > 50\text{Jy}$ and $\delta > -30^\circ$ (Henkel, Wouterloot & Bally 1986) as well as sources observed by Braine et al. (1993) in the CO (1–0) and (2–1) transitions (with the IRAM 30-m telescope) if integrated intensities are $\geq 10\text{K km s}^{-1}$.

The second sub-sample consists of 32 galaxies from a volume limited sample ($V < 7000\text{ km s}^{-1}$) of all Seyfert galaxies and low-ionization nuclear emission-line regions (LINERs) in Huchra’s catalog of AGN (Huchra 1993) or in the Véron-Cetty & Véron (1991) catalog that are also included in the *Revised Shapley Ames Catalog* (RSA) and that are accessible with the HHT (74 in total).

The third sub-sample consists of 25 early type galaxies from Henkel & Wiklind (1997) with CO(1–0) and/or CO(2–1) lines detected. Observations at radio, optical, and X-ray wavelengths have shown that early-type galaxies contain an interstellar medium (ISM) comprising the same components as found in spiral galaxies, but with different mass fractions of the gas components (see also Henkel & Wiklind 1997 for a review).

The fourth sub-sample consists of clearly identified 11 interacting or merging systems, which are mainly luminous infrared galaxies (LIRGs, $10^{11}\text{ L}_\odot \leq L_{\text{FIR}} < 10^{12}\text{ L}_\odot$). The selection is based on their relatively high single dish and/or interferometer CO(1–0) fluxes (see, e.g., Sanders et al. 1991; Gao et al. 1999; Lo et al. 2000, and references therein). These galaxy systems are thought to be at different merging/interaction phases, i.e. at the early (presumably pre-starburst: Arp 303N/S, UGC 8335A/B, NGC 5257/8, Arp 302N/S, Arp 293 and NGC 6670A/B), intermediate (Arp 55, Mrk 848 and NGC 4038/9), or late stages of interaction (NGC 1614, NGC 5256), according to the spatial separation of the respective galaxy pair in each system. The two core positions of five early mergers (not Arp 293) as well as NGC 4038/9 (the Antennae) were measured separately because they are spatially resolved by our 22'' beam (see §3). Including these double core positions, the fourth sub-sample contains a total of 17 individual sources. For the central position of Arp 302, “Arp 302 center” (Table 1), see also §A.2.

The members of the fifth sub-sample are prominent OH megamaser galaxies, including 4 ultraluminous infrared galaxies (ULIRGs, $L_{\text{FIR}} \geq 10^{12}\text{ L}_\odot$: IRAS 17208-0014, Mrk 231, Mrk 273, and Arp 220) and 2 LIRGs (III ZW 35 and NGC 3690B), all of them being late mergers (following the classification outlined above), except NGC 3690B, which is “early”.

2.2. Sample properties as a whole

2.2.1. The IRAS fluxes

98 of our sample galaxies are part of the *IRAS Revised Bright Galaxy Sample* (RGBS) by Sanders et al.

⁸ The NASA/IPAC Extragalactic Database (NED) is operated by the Jet Propulsion Laboratory, California Institute of Technology, under contract with the National Aeronautics and Space Administration.

⁹ HyperLEDA database: <http://leda.univ-lyon1.fr>

(2003), which provides revised IRAS fluxes. 23 of these were determined with particularly high precision, also profiting from the HIRES imaging reconstruction technique (Surace et al. 2004). With the higher spatial resolution obtained by this technique, four of our galaxy pairs (i.e., Arp 303N/S, NGC 5257/8, UGC 8335A/B, and Arp 302N/S) are resolved and fluxes for each individual galaxy are available. The mid- to far-IR emission of the NGC 4038/9 system (the Antennae) originates predominantly from the overlap region where the disks of two galaxies interact (e.g., Schulz et al. 2007). Flux densities directly obtained from IRAS catalogs, i.e. *the IRAS Point Source Catalog* (PSC; Joint IRAS Science Working Group 1988), *the IRAS Explanatory Supplement* (Beichman et al. 1988), and *the IRAS Faint Source Catalog* (FSC; Moshir et al. 1992) were taken for the rest of the sample. We then applied the flux densities to calculate the FIR luminosity ($L_{\text{FIR}} = L(40\text{--}400\ \mu\text{m})$), following Moshir et al. (1992), and the $60\ \mu\text{m}/100\ \mu\text{m}$ color temperature (T_{dust}), assuming an emissivity that is proportional to the frequency ν . Two galaxies, IC 750 and NGC 4138, were not observed by IRAS.

2.2.2. Galaxy classifications

With improved observations, galaxy classifications may have to be modified in some cases. We have used the NED classifications from August 2008 as standard throughout the paper. While Seyferts/LINERs can be directly recognized from NED, starbursts are not explicitly indicated. There exists a variety of definitions of the starburst phenomenon in the literature, which have been reviewed by, e.g., Heckman (2005) and Kennicutt et al. (2005). A starburst can be defined in terms of its absolute star forming rate (SFR), its SFR surface density (the SFR per unit area), or if its SFR exceeds an average value from the past by a fixed amount. The situation is further complicated by the choice of the respective SFR tracer like, e.g., the ultraviolet emission, the far infrared emission, or the radio continuum. Spectroscopic tracers like recombination lines (e.g., H α) have also been frequently used.

Here we select L_{FIR} as *the* measure of the SFR and define a starburst galaxy in terms of its SFR surface density. Lacking high resolution information, we use with the isophotal diameter D_{25} the ratio L_{FIR}/D_{25}^2 to determine the SFR surface density and classify targets with $\log(L_{\text{FIR}}/D_{25}^2) \geq 7.25\ L_{\odot}\ \text{kpc}^{-2}$ as starburst galaxies. This parameter is plotted as a function of $\log L_{\text{FIR}}$ in Fig. 1, where the boundary between starburst and non-starburst galaxies is marked by a dashed horizontal line. The borderline was chosen to ensure that most of the well known starburst galaxies are properly classified. Galaxies, which were classified as starbursts in the literature (regardless of the details of the definition), are marked as stars. While all (U)LIRGs and most of the well known starburst galaxies are well above the borderline, there are 19 galaxies that were “misclassified” (following our definition) as non-starbursts and 7 galaxies that were “misclassified” as starbursts. NGC 253, a typical starburst galaxy, and IC 342, a galaxy similar to our Milky Way galaxy, are part of Fig. 1 to ensure that the classification method is correct. Both are located in the expected zone. The starburst sub-sample, selected as such, includes 24

classical starbursts, 16 Seyfert composites, 13 starburst supported LINERs, 3 dwarf starburst galaxies ($M_B > -18$; e.g., NGC 1569), and all 28 (U)LIRGs, or in total 77 galaxies (some of these galaxies have more than two assignments).

Characterized by FIR luminosity and nuclear activity, the entire sample consists of 4 ULIRGs, 24 LIRGs, 45 Seyferts, 45 LINERs, 49 starbursts neither being ULIRGs nor LIRGs, and 11 “normal” galaxies. Note that one object may be part of more than one sub-sample. The sample classification is presented in more detail in Table 2.

The sub-sample of Seyferts is severely biased to Seyfert 2 galaxies, with only 7 galaxies classified as Seyfert 1. Although individually not satisfying the LIRG criterion $10^{11}\ L_{\odot} \leq L_{\text{FIR}} < 10^{12}\ L_{\odot}$, Arp 303 S and N are both classified as LIRGs since the system as a whole meets the LIRG criterion. There are 16 Seyferts that are also classified as LINERs. Hence there is a total of 74 AGN in our sample. Excluding those overlapping with the starburst and (U)LIRG sub-samples, there remain 35 galaxies which show “pure” AGN activity.

The sample can also be broken down by Hubble types. We observed 42 early-type (including 19 lenticulars, 2 ellipticals, 1 cD, and 20 early-type spirals) and 54 late-type galaxies (5 irregulars and 49 late type spirals), with a Hubble type index of $t = 3$ (or Sb in the RC3, de Vaucouleurs et al. 1991; Paturel et al. 2003) being used as the dividing line ($t < 3$: early type, $t \geq 3$: late type). Because of their peculiar morphology, the 28 (U)LIRGs of our sample have not been included. Concerning the presence and the strength of a bar, the sample covers 42 SA (unbarred), 31 SAB (weakly barred) and 25 SB (barred) galaxies. It also comprises 11 Virgo cluster galaxies and 8 dwarf galaxies ($M_B > -18$).

2.2.3. The sample distribution

In Fig. 2 we present some basic properties of the entire sample of 125 observed galaxies, i.e. the distribution of Hubble type, FIR luminosity (L_{FIR}), $60\ \mu\text{m}/100\ \mu\text{m}$ dust color temperature (T_{dust}), distance (d_p), optical angular size (D_{25} in arcmin), optical linear size (D_{25} in kpc), inclination angle (i), and absolute B-band magnitude (M_B). Our sub-samples cover almost all types of galaxies, with most of them belonging to Hubble types 3 – 5 (see de Vaucouleurs et al. 1991), corresponding to the revised (de Vaucouleurs) morphological types Sb–Sbc–Sc. The far-infrared luminosity of our sample spans almost 5 orders of magnitude, $\log(L_{\text{FIR}}/L_{\odot}) \sim 7.5\text{--}12.4$, with a median value of $\log(L_{\text{FIR}}/L_{\odot}) \sim 10.2$, which is very close to the total far-infrared luminosity of the Galaxy (e.g., Beichman 1987). The dust color temperature T_{dust} , obtained by assuming an emissivity proportional to ν (see footnote to Table 1), varies between 24 K and 50 K, with a peak at about 35 K. The distance distribution shows a strong peak at 10–20 Mpc, where our beam size of $22''$ (see § 3) corresponds to a linear scale of about 1–2 kpc. These are typical sizes for circumnuclear starbursts. The optical diameter is in a range between 0.4 to 18.6 arcmin on an angular and 1.3 to 78 kpc on a linear scale, with values of 25–40 kpc being most typical. About 70% of our sample galaxies have an optical diameter (D_{25}) smaller than 5 arcmin, and the strong peak at 1–2 arcmin is due to the merging sequence sub-sample (see § 2.1). The in-

clination angle is broadly distributed between $\sim 30^\circ$ and 90° . There are only few galaxies with inclinations below $i \sim 30^\circ$. Our sample spans a B-band absolute magnitude range from -16.4 to -22.6 , the majority having with $M_B < -20$ a high luminosity.

3. OBSERVATIONS

All the CO(3–2) observations were conducted with the 10-m Heinrich-Hertz Telescope (HHT) on Mt. Graham/Arizona with a beamwidth of $22''$ ¹⁰. Most of our galaxies were observed during Feb., Apr. and Nov. 1999, Jan. and Mar. 2000. The majority of the merging/interacting galaxies was observed in Mar. 2003, Mar. 2004 and Mar. 2005. In all cases, the same dual channel 345 GHz SIS (Superconductor-Insulator-Superconductor) receiver was employed. Spectral profiles were obtained with two acousto-optical spectrometers (AOSs), each with 2048 channels (channel spacing ~ 480 kHz, frequency resolution ~ 930 kHz, corresponding to a velocity resolution of ~ 0.8 km s⁻¹) and a total bandwidth of 1 GHz.

Spectra were taken using a wobbling (2 Hz) secondary mirror with beam throws of $\pm 120''$ to $\pm 240''$ in azimuth. Scans obtained with reference positions on either side of the source were coadded to ensure flat baselines. Receiver temperatures were of order of 170 K and system temperatures were ~ 900 K on a T_A^* scale, respectively.

Calibration at submillimeter wavelengths is often difficult, especially for extragalactic observations, and needs to be carefully checked. The receivers were sensitive to both sidebands. Any imbalance in the gains of the lower and upper sideband would thus lead to calibration errors. To account for this, galactic calibration sources (e.g. Orion-KL, IRC+10216, Sgr B2, G34.3, and W51, depending on availability at the time of observation) were observed prior to the target source with the same receiver tuning setup. Published spectral line survey data in the 345 GHz band were used for intensity calibrations, e.g. Schilke et al. (1997) for Orion-KL, Groesbeck et al. (1994) for IRC+10216, Sutton et al. (1991) for Sgr B2, Hatchell et al. (1998) for G34.3, and Wang et al. (1994) for W51. Pointing and focus were carefully checked before the calibration spectra were taken. Nevertheless, the absolute calibration error could be as large as $\pm 30\%$ (see § 4.3).

After a first order (or second order in very few cases) baseline subtraction, the antenna temperature T_A^* was converted to main beam brightness temperature T_{mb} via $T_{\text{mb}} = T_A^* (F_{\text{eff}}/B_{\text{eff}})$ (see, Downes 1989). The main beam efficiency, B_{eff} , was 0.5 at 345 GHz, as obtained from measurements of Saturn, and the forward hemisphere efficiencies, F_{eff} , was 0.9 (see also Mao et al. 2002).

To reduce as much as possible the number of receiver tunings, we used the same tuning setup to observe as many galaxies as possible with similar velocities. Therefore, in some cases the line is detected well outside the center of the spectrum and sometimes even reaches the band edge of the backend, in which case only a zero order baseline subtraction was performed. Additionally, in

a few galaxies like Mrk 273, NGC 6240, IRAS 17208-0014, Arp 220, and Arp 302N, the full width to zero power of the line is as wide as ~ 1000 km s⁻¹ (as shown in wide band interferometer data; e.g., Scoville et al. 1997), which exceeds the bandwidth of the backend used for our observations. The intensities in such cases can only be considered as lower limits, unless some concatenated spectra were obtained, as in the case of Arp 220 and Arp 302N.

4. RESULTS

4.1. Spectra and line parameters

Figure 3 shows the CO(3–2) spectra (on a T_{mb} scale) towards all detected galaxies. The line parameters or the upper limits in case of non-detections are given in Table 3. The spectra have been smoothed to a velocity resolution of ~ 3 – 20 km s⁻¹ in order to show the emission features more prominently. Spectra with the velocity integrated intensity $I_{32} = I_{\text{CO}(3-2)} = \int T_{\text{mb}} dv$ larger than three times the r.m.s noise are considered to be detected. We have determined the integrated line intensity, the radial velocity and the line width using either Gaussian fits to the lines, or the moments of the spectra in the case of non-Gaussian line profiles. Spectra of Arp 220 and Arp 302N were concatenated from two different velocity setups to cover the full velocity ranges that exceed the bandwidth of the backend. Of the observed 125 galaxies, 114 were detected, among which CO(3–2) data of 65 galaxies are reported here for the first time. For spectra with a signal to noise ratio of less than 3, an upper limit is derived using $I_{32} < 3\sigma (\Delta V_{10} \delta v)^{1/2}$, where σ is the r.m.s noise in T_{mb} for a single channel, and ΔV_{10} represents the full linewidth taken from the FCRAO CO(1–0) survey results (Young et al. 1995; Kenney et al. 1988) or arbitrarily set to 400 km s⁻¹ if there was no CO(1–0) data available. δv denotes the channel spacing.

The CO(3–2) luminosity, $L_{\text{CO}(3-2)}$ in units of $\text{K km s}^{-1} \text{ pc}^2$, is calculated within our $22''$ beam by

$$L_{\text{CO}(3-2)} = [\pi/(4\ln 2)] \Theta_{\text{mb}}^2 I_{32} d_L^2 (1+z)^{-3}, \quad (1)$$

where $\Theta_{\text{mb}} = 22'' = 1.067 \times 10^{-4}$ rad is the full width to half maximum (FWHM) main beam size of the HHT at 345 GHz, $d_L = d_c(1+z)$ is the luminosity distance in pc (d_p : proper distance in pc, see footnote to Table), and $z = v_{\text{hel}}/c$ denotes the redshift. The CO(1–0) luminosity is derived similarly (see footnotes in Table 3). Because of identical beam sizes ($22''$), the averaged intensity ratio between the $J=3-2$ and $1-0$ CO lines, $R_{31} = I_{\text{CO}(3-2)}/I_{\text{CO}(1-0)}$, is calculated for galaxies with available IRAM-30m CO(1–0). For galaxies with CO(1–0) data from other telescopes, upper or lower limits are given for R_{31} , depending on the CO(1–0) beam size.

4.2. Detection rates and non-detections

Our CO(3–2) detection rates are 91% (10/11), 86% (64/74), 100% (49/49), and 100% (28/28) in normal, Seyfert/LINER, starburst galaxies, and (U)LIRGs, respectively, or about 90% in total. Fortuitously, both the total number and the detection rate, 89% (39/45), are the same for the Seyferts and LINERs. Those sample galaxies that are known to host 22 GHz H₂O and/or 18 cm OH masers are all detected in CO(3–2). For the Virgo

¹⁰ The HHT was operated by the Submillimeter Telescope Observatory on behalf of Steward Observatory and the Max-Planck-Institut für Radioastronomie.

Cluster galaxies, dwarf galaxies, early type and late-type galaxies (see §2.2.2) the detection rates are 82% (9/11), 75% (6/8), 78% (18/23) and 94% (46/49), respectively. Note again that we adopted the NED based classification, which may suffer in some cases from ambiguities.

Eleven of our sample galaxies were not detected in CO(3–2) according to our detection criteria mentioned above. Their CO(1–0) intensity is weak on average ($< 20 \text{ K km s}^{-1}$), with the only exception of NGC 4438 where a relatively strong ($\sim 70 \text{ K km s}^{-1}$) CO(1–0) intensity was reported. NGC 4438, together with NGC 2841 and NGC 5866 were, however, observed at poor weather conditions. NGC 7077 is considered to be a tentative detection, since the central velocity differs by about 140 km s^{-1} from that of the CO(1–0) line, while its integrated intensity marginally satisfies the detection criteria with an S/N ratio of 4σ . One of our non-detections, NGC 855, a dwarf elliptical, was detected by Nakanishi et al. (2007) after a deep integration. The reported intensity is below our 2σ level and therefore well below our detection limit.

It is interesting to note that, except for one dwarf elliptical (NGC 855), all the rest of the non-detections are AGN hosts (either Seyferts or LINERs), and are mostly early type galaxies (7 lenticulars and 3 spirals). This is suggestive of a possible destruction of molecular gas reservoirs by AGN feedback, and consequently a suppression of star formation in early type galaxies (see, e.g., Schawinski et al. 2007). Except for 3 SAB galaxies, the non-detections were all obtained from unbarred galaxies.

4.3. Consistency of the observed CO intensities

As already mentioned in §3, calibration uncertainties may rise up to $\pm 30\%$. Furthermore, with a $22''$ beam, any shift $\gtrsim 5''$ could yield significant discrepancies in both line shape and intensity. This could further increase the uncertainties of measured absolute intensities and requires a detailed comparison with data from previous surveys with respect to both intensity and line shape. The large sample analyzed here brings us into the unique position to test not only the quality of our own data but also that of previously studied samples. The comparison of spectroscopic results is given in the Appendix and starts with previous measurements also obtained with a 10-m sized telescope (§A.1) and continues with the inclusion of data from the James Clerk Maxwell 15-m telescope (JCMT, §A.2).

In general, our results are consistent with published data. The inconsistencies found for a few individual sources can be attributed to errors of pointing, calibration and baseline subtraction (especially for broad spectra) which are difficult to quantify. A typical error of $\sim 30\%$ is not unusual even for millimeter observations. Therefore, the inconsistencies shown in the Appendix are within expected ranges, still leaving space for significant improvements, possibly obtained by mapping the galaxy cores. Among the sources with large discrepancies in intensities ($> 50\%$), four (NGC 891, NGC 3079, M 83, and Arp 220) have been reported with both weaker and stronger intensities in the literature, leaving our intensities close to the medium values. Among galaxies with published CO(3–2) maps available, large discrepancies are found for four out of a total of twelve sources

(NGC 891, NGC 2146, NGC 3593, and NGC 4631). Skewed profiles appear in a few spectra of Fig. 3 and are most likely caused by pointing errors. Some galaxies show, however, off-centered CO emission, and the profiles from the nuclear regions are thus not necessarily symmetric. Considering all these uncertainties and also to keep the uniformity of the data set, we will exclusively use our data for the following discussion. Given the large sample, a few galaxies with relatively large calibration errors should not affect the overall correlations (see also §5.2.2).

5. DISCUSSION

5.1. The CO(3–2)/(1–0) Line Intensity Ratio

The beam averaged integrated intensity ratio, $R_{31} = I_{\text{CO}(3-2)}/I_{\text{CO}(1-0)}$, can serve as an indicator of the molecular gas excitation since the ratio is sensitive to the temperature and density of the molecular gas (e.g., Mauersberger et al. 1999). Although the excitation status of the molecular gas cannot be accurately determined with only two optically thick transitions, i.e. CO(3–2) and (1–0), we can use R_{31} to constrain the molecular gas temperature and density with either Large Velocity Gradient (LVG) or Photon-Dominated Region (PDR) models. While it is likely that R_{31} is varying within the region observed (see, e.g., Dumke et al. 2001, who find that CO(3–2) is more centrally concentrated), our R_{31} values provide a representative average over the size of the beam.

5.1.1. Molecular Gas Excitation Traced by R_{31}

Considering $\Lambda = [n(\text{CO})/n(\text{H}_2)]/(dv/dr) = 10^{-4}$ and $10^{-5} (\text{km s}^{-1}/\text{pc})^{-1}$, consistent with Mauersberger et al. (1999), one-component LVG calculations (c.f. Scoville & Solomon 1974; Henkel et al. 1980; Mao et al. 2000) with the recent collision rates of Flower (2001) show that $R_{31} \geq 1$ corresponds to $T_k \gtrsim 60 \text{ K}$ and an H_2 density of $n(\text{H}_2) \gtrsim 10^{3.5} \text{ cm}^{-3}$. Both of these values are larger than those given in Mauersberger et al. (1999), where old collision rates were used. For the extreme case of $R_{31} = 1.9$, a gas temperature of at least $\sim 200 \text{ K}$ is required. A ratio of $R_{31} = 0.2$ would instead indicate $n(\text{H}_2) < 300 \text{ cm}^{-3}$ for $\Lambda = 10^{-4} (\text{km s}^{-1}/\text{pc})^{-1}$, or $n(\text{H}_2) < 2500 \text{ cm}^{-3}$ for $\Lambda = 10^{-5} (\text{km s}^{-1}/\text{pc})^{-1}$ if $T_k = 20 - 60 \text{ K}$.

The thermal budget of the interstellar molecular gas in starburst regions can be described predominantly in terms of a PDR scenario (see, e.g., Hollenbach & Tielens 1997; Mao et al. 2000; Schulz et al. 2007). If we take a typical strength of the incident far-ultraviolet (FUV) radiation field, $G_0 \sim 10^{2.8-3.9}$ (in units of the local galactic flux, $1.6 \times 10^{-3} \text{ erg s}^{-1} \text{ cm}^{-2}$, c.f. Mao et al. 2000, and references therein), as for the starburst in M82, the standard PDR model (Kaufman et al. 1999) results in $n(\text{H}_2) = 10^{3.9-4.9} \text{ cm}^{-3}$ and cloud surface temperatures of $300 - 600 \text{ K}$ for $R_{31} = 1.0 - 1.6$.

Among our 114 galaxies with detected CO(3–2) emission, 68 have published IRAM-30m CO(1–0) data. These are the best candidates for a comparison (c.f. §4.1) because of matching beam sizes ($22''$). Seven of these galaxies (marked with a superscript † in Col.(10) of Table 3) have been excluded because of a positional discrepancy by $\geq 5''$ (for the coordinates used by us, see

Table 1). Therefore, there remain 61 sources for our analysis. For those galaxies with no available IRAM-30m CO(1–0) data but with measurements from other telescopes (i.e. NRAO-12m, FCRAO-14m, SEST-15m, Onsala-20m and NRO-45m), upper or lower limits were estimated. The results are listed in Table 3.

Figure 4 shows the distribution of the R_{31} ratio of the 61 sources. The distribution has a prominent peak around 0.5, which is the typical value in the spiral arms of the Galactic disk (e.g., Oka et al. 2007), and an additional minor excess at about 1.5, which is a sign of highly excited gas as found in the Central Molecular Zone (CMZ) of the Galaxy (for the Sgr A region see, e.g., Oka et al. 2007). The values of R_{31} range widely from 0.2 to 1.9 with a mean of 0.81 ± 0.06 (cf. Mauersberger et al. 1999; Yao et al. 2003), the error being the standard error of the mean. The R_{31} distribution is deviating from a normal one, so that (following Chebyshev’s inequality) probabilities within a given range of standard deviations are expected to be moderately lower than those in the case of a normal distribution.

There are 18 sources with $R_{31} > 1$, indicative of very high excitation combined with low optical depth. As expected, these are mostly starbursts or (U)LIRGs, since such high R_{31} ratio gas may arise predominantly from UV-irradiated surfaces of molecular clouds or shocked regions, possibly generated by the interaction with supernova expansion waves (Oka et al. 2007, and references therein), which are fairly common in starburst regions.

NGC 3310, a starburst galaxy with an exceptionally high CO(2–1)/(1–0) intensity ratio (2.6 ± 0.6) as found by Braine & Combes (1992), shows also the highest R_{31} ratio (1.9 ± 0.52), confirming the peculiar physical conditions of the molecular gas in its central region. Enhanced massive star formation triggered by a recent merging event with a gas-rich galaxy (e.g. Balick & Heckman 1981; Kregel & Sancisi 2001) is most likely responsible for this peculiar value.

Molecular gas with a high R_{31} ratio does not *always* need high excitation and has also been found in the Galactic interarm regions where low density gas dominates (Oka et al. 2007). However, such interarm regions should not dominate the overall CO emission of a spiral galaxy. Alternatively, a warm opaque cloud veiled by a cool foreground layer of low density, which absorbs the CO(1–0) but not the CO(3–2) emission, could also raise the R_{31} ratio to an exceptional level without participation of highly excited gas of low opacity (see below).

Table 4 summarizes the results related to R_{31} for the different galaxy types outlined in §2.1. In the following, we will discuss which properties of the galaxies observed may most efficiently affect the determined R_{31} ratios.

5.1.2. Correlations between R_{31} and galaxy properties

In Fig. 5, R_{31} is shown as a function of Hubble type, distance (or linear beam size), inclination, FIR luminosity, $60\mu\text{m}/100\mu\text{m}$ dust color temperature, and optical size (D_{25}).

1) *Hubble type* – There is no correlation between R_{31} and Hubble type (Fig. 5a, but see Nakanishi et al. 2007 for elliptical galaxies). The bulk of the CO emission in the majority of galaxies arises from the central region, which is largely decoupled from the Hubble type and the shape of the large scale disks (Kennicutt 1998).

2) *Projected beam size* – Fig. 5b shows no correlation, agreeing with Yao et al. (2003) on a similar analysis for their sample. Such a lack of correlation also holds within a given Hubble type of galaxies. It may imply that toward the nearby galaxies we see exclusively the nuclear region, while in the more distant more luminous galaxies the central regions become so dominant that the larger projected beam size is not important any more.

3) *Inclination* – Inclination may affect the observed R_{31} , since we tend to include more low excitation gas from the outer disk into the observing beam for galaxies seen more edge-on, thus lowering R_{31} . Nevertheless, Fig. 5c shows no strong trend between R_{31} and the cosine of the inclination. However, the upper envelope of the R_{31} distribution as well as the number of sources with high R_{31} increase with decreasing inclination. While this agrees with the expected trend, the correlation is not significant.

4) *FIR luminosity and color temperature of the dust* – The FIR luminosity and the temperature of the dust are expected to be correlated with the molecular gas excitation, if dust and gas are coupled. In Figs. 5d and e we therefore correlate R_{31} with L_{FIR} and the $60\mu\text{m}/100\mu\text{m}$ dust color temperature (T_{dust}). Although there may be a weak trend with T_{dust} , similar to that mentioned above for the inclination, no significant correlation is evident. This could be partially attributed to the fact that we plot the global dust properties against the rather localized line ratio R_{31} emphasizing the nuclear regions. In Fig. 5f we also plot R_{31} as a function of L_{FIR}/D_{25}^2 , a measure of the SFR per unit area, but again there is no convincing correlation (see also Yao et al. 2003). This can be interpreted in the sense that star formation is a locally confined activity.

5) *Nuclear activity* – In addition to star formation, AGN may also provide a source of heating for the surrounding molecular gas (see, e.g., Matsushita et al. 2004). As summarized in Table 4, the average R_{31} ratios are 0.65 ± 0.08 and 0.82 ± 0.12 for LINERs and Seyferts, respectively, or 0.78 ± 0.09 for “pure” AGN. Although being larger than in normal galaxies (0.61 ± 0.16), these values are similar to or lower than the mean value of the entire sample (0.81 ± 0.06). This may be caused by the fact that AGN activity is spatially too much confined for the currently achieved angular resolution.

On the other hand, starbursts and (U)LIRGs do show higher average R_{31} ratios (0.89 ± 0.11 and 0.96 ± 0.14 , respectively). Among the 18 galaxies with R_{31} in excess of unity, 14 belong to starbursts. This indicates that the presence of a nuclear starburst is a major reason for a high, beam averaged R_{31} value.

6) *Bars* – Bars are expected to enhance the gas flow toward the center of galaxies, building up the nuclear gas reservoir to maintain nuclear activity and affecting the molecular gas excitation. We find that R_{31} is higher in barred SB and SAB galaxies (0.88 ± 0.15 and 0.80 ± 0.11 , respectively) than in non-barred SA galaxies (0.62 ± 0.10). This and the fact that there are no SB galaxies and only three SAB galaxies among our 11 CO(3–2) non-detections, indicates that the presence of bars can not only enhance the CO gas excitation, but is also increasing the central molecular gas reservoir.

7) *The merging sequence* – Most of the galaxies in the merging sequence sub-sample have no corresponding

IRAM CO(1–0) data. However, in one of the intermediate mergers, the Antennae, we do not see a significant enhancement of CO(3–2), with R_{31} being 0.7, 0.3 and 0.8 for NGC 4038, NGC 4039 and the overlap region, while the mean ratio of the “late” mergers NGC 1614, Mrk 231, Arp 220, and IRAS 17208–0014 is 1.0 ± 0.2 . This is consistent with the result of Leech et al. (2010) who find a weak correlation based on CO(3–2) data from the JCMT.

In summary, while there is significant dispersion between individual objects of a given type, targets hosting an AGN may show higher R_{31} values than “normal” galaxies, while R_{31} ratios are highest in starburst and barred galaxies. Surprisingly, significant correlations of R_{31} with other galaxy properties are not found.

5.2. FIR-to-CO luminosity correlations and star formation laws

The FIR luminosity (as a measure of the SFR in galaxies) is correlated with the CO luminosity (a measure of the total molecular content). Based on the scaling relation $\text{SFR} \propto n_{\text{gas}}^N$, this can be expressed in terms of the so-called Kennicutt-Schmidt law (hereafter KS law; Schmidt 1959; Kennicutt 1998), which connects the SFR per area with the total gas surface density, i.e. $\Sigma_{\text{SFR}} \sim \Sigma_{\text{gas}}^N$, with $N = 1.4 \pm 0.15$. The empirical evaluation of the molecular KS law is, however, tracer-dependent, and molecular line tracers with different critical densities may give different correlations with sub-linear ($s < 1$), linear ($s = 1$), or super-linear ($s > 1$) correlation indices, which differ from N (e.g., Kennicutt 1998; Gao & Solomon 2004a,b; Baan et al. 2008; Bussmann et al. 2008).

Recent models to interpret the various observed correlation indices in a uniform way (Krumholz & Thompson 2007; Narayanan et al. 2008) assume that s depends on the cloud’s gas mass above the critical density of the observed molecular transition. The super-linear $\text{SFR}-L_{\text{CO}(1-0)}$ correlation is caused by the fact that the gas density is on average higher than the CO(1–0) line’s critical density, thermalizing most of the CO(1–0) emission. The sub-linear $\text{SFR}-L_{\text{HCN}(3-2)}$ correlation (Bussmann et al. 2008) is a result of a small fraction of thermal emission as the critical density of the HCN $J=3-2$ transition is high ($n(\text{H}_2) \sim 10^7 \text{ cm}^{-3}$). Observational support for such models is, however, still fragile given the large uncertainties in (sub)millimeter molecular line calibration (§A.1 and A.2) and additional problems mentioned below. In the following, we will first address some of these problems and will then derive the corresponding correlations from our data.

5.2.1. Possible problems in the correlation analysis

For pointed CO observations, as in our case, a direct power law correlation of the nuclear CO luminosity with the global FIR luminosity could be misleading because these two quantities refer to different spatial scales. To evade such a situation, one should ideally obtain extended CO maps to measure the entire molecular gas content for a large sample of galaxies with various Hubble types and FIR luminosity ranges. Full maps of such a large sample of galaxies in CO(3–2) are, however, not yet available.

Yao et al. (2003) employed an alternative way in scaling down the total FIR luminosity as obtained by the

IRAS data to the volume marked by the angular size of the CO observations. The scaling factor is determined by the peak-to-total flux density ratio derived from the corresponding 850 μm submillimeter continuum images. The basic assumption for such a technique to be applicable is that the FIR brightness distribution is similar to that of the 850 μm submillimeter continuum. This is, however, most likely not the case since the FIR emission measured by the IRAS satellite is only sensitive to warm dust ($T_{\text{dust}} \gtrsim 30 \text{ K}$), while the submillimeter continuum also traces dust at cooler color temperatures. In most galaxies, this cooler component dominates. Therefore, the FIR emission is expected to be much more centrally concentrated than the submillimeter emission, especially in the case of nuclear starbursts. Indeed, even the 200 μm continuum emission has already shown significant cold dust at large galactocentric radii (e.g., Alton et al. 1998; Kramer et al. 2010).

Another important aspect is the linear regression fit itself. Published correlation studies sometimes use $L_{\text{CO}}-L_{\text{FIR}}$ and sometimes $L_{\text{FIR}}-L_{\text{CO}}$. Caution has to be exercised, however, in comparing these two approaches. Simply taking an inverse slope (i.e., $1/s$ instead of s) is not appropriate because the standard linear regression fit assumes that X values are exactly correct, and that errors or variability only affect the Y values. Hence the regression of X on Y is different from the regression of Y on X . To determine the line dependent parameter s in analogy to N (§5.2), line luminosities and FIR luminosities must be plotted along the x- and y-axes, respectively. Standard regression fits from figures with inverted axes (as, e.g., displayed by Yao et al. 2003; Baan et al. 2008) cannot be used. There is, however, a way to account for errors along both axes. For this, the publicly available Monte Carlo Markov Chain fitting packages of Kelly (2007) have been developed.

5.2.2. The FIR-to-CO correlation

In Fig. 6, we present the correlation between the nuclear CO line luminosity and the global FIR luminosity L_{FIR} . We performed the fit in both ways, with and without the method introduced by Kelly (2007), considering uncertainties along both axes in the latter case. However, slopes derived with the Kelly packages are (within a percent) the same as those obtained with the unweighted linear regression fits. This is perhaps due to the large number and small intrinsic scatter of our data along both axes in the log-log plots. In the following we will therefore use the unweighted linear regression fits.

Intriguingly, both nuclear CO(3–2) and CO(1–0) line luminosities are tightly correlated to the global FIR luminosity, and our unweighted linear regression fits result in almost identical slopes slightly below unity, $s = 0.87 \pm 0.03$ and 0.87 ± 0.05 for CO(3–2) and CO(1–0), respectively. To account for the fitting problems when exchanging CO and FIR luminosities (§5.2.1), we note that the unweighted linear regression fit for $L_{\text{CO}}-L_{\text{FIR}}$ results in slopes of 0.96 ± 0.04 and 0.94 ± 0.06 for the CO(3–2) and CO(1–0) luminosities. Both slopes related to CO(3–2) are smaller than unity, and are not simply reciprocal values.

To avoid a bias by a single discrete data point, IC 10, with its by far lowest $L_{\text{CO}(3-2)}$ and L_{FIR} values, is not included in the fits of Fig. 6. Fits including IC 10 give,

however, similar slopes of 0.88 ± 0.03 and 0.86 ± 0.04 for CO(3–2) and (1–0), respectively. A fit is also performed replacing four questionable CO(3–2) intensities by the corresponding peak intensities obtained from maps (see the discussion of the mapped sources in §A.1). The new fit gives the same slope, $s = 0.87 \pm 0.04$. This is not unexpected because the number of these galaxies is small with respect to that of the entire sample.

Our slopes are consistent with that derived from 14 local (U)LIRGs (Iono et al. 2009) but differ from those of Yao et al. (2003), who obtained $L_{\text{CO}}(\text{y-axis})-L_{\text{FIR}}(\text{x-axis})$ slopes with scaled FIR luminosities (§5.2.1) well below unity (0.70 and 0.58 for CO(3–2) and (1–0), respectively; see also their Fig. 2). However, using instead the uncorrected FIR luminosities, the slopes become 1.00 and 0.94, respectively, very close to our results.

5.2.3. On the angular size dependence of the correlation

Instead of following Yao et al. (2003) and scaling down the FIR fluxes to the area of the CO observations, we can also test our results by defining different D_{25} ranges, assuming that galaxies with similar optical angular sizes have similar central (22'') to total integrated CO intensity ratios. This assumption is based on the fact that the diameter of the CO(1–0)-emitting region D_{CO} is found to be correlated with the optical diameter D_{25} as $D_{\text{CO}}/D_{25} \approx 0.5$ (Young et al. 1995). The CO(3–2) emission may be more centrally concentrated than the CO(1–0) emission (Dumke et al. 2001) but may follow a similar relation. In Fig. 7 we compare correlations of CO-to-FIR luminosities with our CO(3–2) data (panel a)) as well as the CO(1–0) data from the IRAM-30m telescope (panel b)) and from the FCRAO-14m/NRAO-12m antennas (panel c)) dividing our sample galaxies into three groups: 1) $D_{25} \leq 2'$ (filled circles), 2) $2' < D_{25} \leq 4'$ (empty triangles) and 3) $4' < D_{25} \leq 18'$ (crosses). Corresponding slopes (s) and correlation coefficients (r) of linear regression fits are also given. For a constant D_{CO}/D_{25} ratio the resulting slopes should be close to the case of FIR and CO emission arising from the same region.

The three groups of galaxies show different correlations, irrespective of the CO transition studied. The compact galaxies show slopes of order 1.0–1.1, the intermediate sample is characterized by $s \sim 0.8$ –0.9, and the extended sources have slopes of 0.6–0.7, all with uncertainties in the range 0.05–0.10. For galaxies in the first group, which includes most of the (U)LIRGs and some other galaxies at large distance, most of the CO emission is expected to be covered by the observing beam. For galaxies in the second and third group, the CO(3–2) emission should be somewhat or much more extended but within a given group the scaling factor of the total-to-central (22'') integrated intensities is expected to be similar.

In summary, and without having to assume equal spatial distributions of the CO(3–2) and (1–0) emission, we obtain rising slopes s with increasing compactness of the observed targets. This can be interpreted in terms of the relationship between molecular line emission and gas density, anchored by the underlying KS law (Gao & Solomon 2004b; Krumholz & Thompson 2007; Narayanan et al. 2008; Busmann et al. 2008) as outlined in §5.2. The distant more compact galaxies, many

of them (U)LIRGs, possess in the average denser gas than the more nearby targets, so that their emission is more thermalized, yielding a higher slope. Nevertheless, the roughly linear or sublinear correlations are indicative of a significant fraction of molecular gas with densities lower than the critical density of the tracer used. This is comprehensible in the case of CO(3–2) with its high critical density of $\sim 10^5 \text{ cm}^{-3}$, as the bulk of the nuclear CO emission should arise from a more diffuse medium ($n(\text{H}_2) \sim 10^{3-4} \text{ cm}^{-3}$; e.g., Mauersberger et al. 1999; Mao et al. 2000). It is, however, difficult to interpret the correlation in the same way with CO(1–0) because the density of the bulk of the nuclear molecular gas may not be lower than $\sim 10^{3.5} \text{ cm}^{-3}$. Clearly, this deserves further study. More beam matching CO(1–0) data, more maps providing a measure of the entire CO(3–2) emission of a galaxy, data from more than two CO transitions, and infrared data of high angular resolution would thus be helpful.

6. CONCLUSIONS

1. CO(3–2) spectra from the central region of a sample of 125 galaxies are presented. With an angular resolution of 22'', CO(3–2) emission is detected in 114 targets. Our survey significantly increases the number of available CO(3–2) data from galaxies and provides a reliable data base for future surveys with higher angular resolution, establishing a bridge to the high J lines observed toward redshifted targets.

2. The CO(3–2)/(1–0) integrated line intensity ratio R_{31} varies widely from 0.2 to 1.9. The line ratio appears to be independent of galaxy properties such as Hubble type and FIR luminosity and only shows tentative, not significant correlations with $60\mu\text{m}/100\mu\text{m}$ dust color temperature and inclination angle.

3. To be consistent with common designations but to use at the same time a clear definition, we have specified the term ‘‘starburst galaxy’’ by the condition $\log [(L_{\text{FIR}}/L_{\odot})/(D_{25}^2/\text{kpc}^2)] > 7.25$. 77 of our sample galaxies show this property, which is a measure of star formation activity per surface area.

4. The average R_{31} ratios are found to be larger in galaxies with nuclear activity (AGN and starbursts) or with bars than in those without. Apparently, these are the galaxies showing enhanced molecular excitation. Most galaxies with a line ratio of $R_{31} \geq 1$ are starbursts. (U)LIRGs have the highest average R_{31} value, which may be caused by particularly vigorous activity triggered by galaxy interaction and merging.

5. The nuclear CO luminosities show a slightly sub-linear correlation with the global FIR luminosity in both the CO(3–2) and the (1–0) lines. Subdividing our sample into several bins with different angular sizes to compensate for the different size of the regions from where CO and FIR emission have been measured reveals significant differences. Compact and thus mostly distant luminous galaxies show the largest slopes, possibly a consequence of relatively high overall molecular densities, yielding larger fractions of thermalized gas. A similar trend for CO(1–0) is more difficult to explain, because this would require densities below $10^{3.5} \text{ cm}^{-3}$.

ACKNOWLEDGEMENT

We wish to thank an anonymous referee for critically reading the manuscript. We also wish to thank the HHT staff for their enthusiastic support of the project and for their flexibility in changing schedules according to variable weather conditions. We also thank Dr. Jiangshui Zhang for his help in preparing some of the tables and Dr. B. Kelly for a latest version of his software package. We acknowledge useful discussions with Drs. M. Dumke and A. Weiß. RQM is partly supported by NSFC under grants 10373025 and 10733030.

APPENDIX

A.1. COMPARISON OF CO(3–2) SPECTRA TAKEN WITH THE SAME ANGULAR RESOLUTION

- 1) A comparison of 22 galaxies with the data by Mauersberger et al. (1999, HHT-M99) shows good agreement within the errors. Eight sources were re-observed at different positions, four of them at positions displaced by more than $10''$ (NGC 3627, NGC 3628, NGC 6946, and NGC 7541), with the new data showing more symmetric profiles and stronger intensities. The significant difference in observed line shapes toward NGC 2146 is likely due to a position offset of $6''$, and the flat-topped profile of Mauersberger et al. (1999) looks more like a line from the center of the galaxy than our sharply peaked profile. For most of the other galaxies (NGC 3227, NGC 3351, NGC 3368, NGC 4414, NGC 4818), our new data show higher quality profiles although the integrated intensities are quite consistent.
- 2) Dumke et al. (2001, HHT-D01) presented extended CO(3–2) maps toward nine of our sample galaxies where we can check the pointing by comparing our line profile with their individual spectra. For Maffei 2, M 82, M 51, and NGC 6946, Dumke et al. (2001) present spectra, which are consistent with ours with respect to both lineshape and intensity. For NGC 3628 and M 83, our profiles and intensities resemble theirs at the $(10'', 0'')$ and $(-10'', 0'')$ offsets, respectively, where the line intensities are about 30% weaker than the peak intensities at their $(0'', 0'')$ positions. Relatively large discrepancies exist for three sources. The line shape of NGC 4631 resembles that given by Dumke et al. (2001) but their intensity is about twice as high. The other two are observed at positions slightly different from the nominal position used by Dumke et al. (2001). Our position of NGC 891 corresponds to their $(-6'', -7'')$ offset position, where their integrated intensity of about 50 K km s^{-1} is tripling our value (17.3 K km s^{-1}). The position we observed for NGC 2146 is $5''$ east of their reference position, but our spectrum looks more like theirs at the $(10'', -10'')$ offset position. At this position, their intensity is about twice as strong as ours. The spectrum by Mauersberger et al. (1999) is consistent with Dumke et al. (2001) with respect to both line shape and intensity, although the nominal positions differ by about $10''$. Our observations of all these three source seem to suffer from large calibration errors, and NGC 2146 may suffer from an additional pointing error.

- 3) Vila-Vilaró et al. (2003, HHT-V02) covered five early type galaxies of our sample, with NGC 404 and NGC 4691 being slightly stronger (by 25% and 5%, respectively than our spectra. NGC 855 and NGC 5666 are non-detections in both data sets (NGC 5666 was a tentative detection in their paper). Our spectrum of NGC 3593 looks more like that of their $(10'', 0'')$ position which gives an intensity twice as strong as ours.
- 4) Narayanan et al. (2005, HHT-N05) observed three of our sample galaxies. While their integrated intensities for NGC 3079 and Arp 220 are about twice as large as our values, IRAS 17208-0014 shows less than half of the strength we got. A detailed check is not possible, however, since their given positions (their Table 1) are erroneous.
- 5) For the six common sources also observed by Bayet et al. (2006, CSO-B06) with the CSO-10m telescope, we find consistent results for NGC 3079, NGC 6946 and the Antennae system. Our intensities of Mrk 231, M83, and Arp 220 are, however, all about twice as large as theirs. Their CO(3–2) spectrum of NGC 4736 looks more symmetric than ours and has an intensity, which is 40% higher.
- 6) Among the five common sources also observed by Komugi et al. (2007, ASTE-K07) with the ASTE-10m telescope, four galaxies (NGC 1068, NGC 1084, NGC 1087 and NGC 7479) were observed at similar (offsets $\leq 6''$) positions and show quite consistent results. The large discrepancy in the case of NGC 157 is due to a position offset of about one telescope beam ($22''$). Our spectra show generally better baselines thanks to the backend, which is twice as wide as theirs.

To evaluate consistencies on a quantitative basis, we define a relative intensity deviation as $\log(I'/I_0)$, where I' is the integrated CO(3–2) intensity obtained from the literature and I_0 is from this work. Figure 8 shows the relative intensity deviations for galaxies with CO(3–2) data available in the articles mentioned above. About 80% of the data points, excluding those observed at nominal position offsets $\gtrsim 5''$ (open squares in Fig. 8), are falling into the ± 0.3 dex deviation limits.

A.2. COMPARISON OF CO(3–2) SPECTRA TAKEN WITH DIFFERENT ANGULAR RESOLUTION

Comparisons with observations at different angular resolution are not straightforward and need to be treated with utmost caution, since the molecular gas is rarely smoothly distributed in galaxies, and any simple scaling could easily become artificial. For the galaxies with more or less known structure, comparisons of line profiles and intensities can, however, still be helpful to check consistency.

In Fig. 9, we compare our results with published CO(3–2) data taken with the JCMT-15m telescope by Yao et al. (2003, JCMT-Y03) and Wilson et al. (2008, JCMT-W08). Two straight lines denote the theoretical relationship of intensities obtained with the JCMT

and HHT assuming point-like (dashed) and uniformly-extended (dotted) structures with respect to the observing beams. Most of the sources are located between these two lines, as expected in case of well calibrated intensities. In general, the JCMT-15m CO(3–2) data tend to yield higher intensities, as expected, given their higher angular resolution. This also holds for M 83 (Muraoka et al. 2009) and NGC 3521 and NGC 3627 (Warren et al. 2010), with the former two galaxies revealing integrated CO(3–2) intensity compatible with our values, while their CO(3–2) emission peak toward the latter is stronger by a factor of 2.5.

Toward the interacting Arp 302 N/S system, Yao et al. (2003) observed a position in between the pair of nuclei, where the CO emission is weak and where we only ob-

tained an upper limit (indicated by the arrow pointing towards the left). This refers to “Arp 302 center” in Tables 1 and 3. We also observed this system at the positions of its two nuclei (i.e., Arp 302 N/S), where emission is stronger. Sources, where JCMT CO(3–2) intensities were derived from maps, are labeled by arrows pointing downwards. Our CO(3–2) intensity of NGC 3690 (or Arp 299 in Wilson et al. 2008) is a sum of NGC 3690 A and B. Differences between the JCMT and our HHT integrated intensities are most pronounced toward Mrk 848 and NGC 5258. While in the case of Mrk 848 this may be due to differences in calibration, the results from NGC 5258 may be caused by an unusual gas morphology (see also Wilson et al. 2008).

REFERENCES

- Albrecht, M., Chini, R., Krügel, E., Müller, S. A. H., & Lemke, R. 2004, *A&A*, 414, 141
- Albrecht, M., Krügel, E., & Chini, R. 2007, *A&A*, 462, 575
- Alton, P. B., et al. 1998, *A&A*, 335, 807
- Baan, W. A., Henkel, C., Loenen, A. F., Baudry, A., & Wiklind, T. 2008, *A&A*, 477, 747
- Baars, J. W. M., & Martin, R. N. 1996, *Rev. Mod. Astro.*, 9, 111
- Balick, B., & Heckman, T. 1981, *A&A*, 96, 271
- Bayet, E., Gerin, M., Phillips, T. G., & Contursi, A. 2006, *A&A*, 460, 467
- Beichman, C. A. 1987, *ARA&A*, 25, 521
- Beichman, C. A., Neugebauer, G., Habing, H. J., Clegg, P. E., & Chester, T. J., eds. 1988, *IRAS Catalogs and Atlases Explanatory Supplement (NASA RP-1190)* (Washington, DC: GPO)
- Benedict, G. F., Howell, D. A., Jørgensen, I., Kenney, J. D. P., & Smith, B. J. 2002, *AJ*, 123, 1411
- Braine, J., & Combes, F. 1992, *A&A*, 264, 433
- Braine, J., Combes, F., Casoli, F., Dupraz, C., Gerin, M., Klein, U., Wielebinski, R., & Brouillet, N. 1993, *A&AS*, 97, 887
- Brunthaler, A., Castangia, P., Tarchi, A., Henkel, C., Reid, M. J., Falcke, H., & Menten, K. M. 2009, *A&A*, 497, 103
- Bussmann, R. S., et al. 2008, *ApJ*, 681, L73
- Casoli, F., Combes, F., Augarde, R., Figon, P., & Martin, J. M. 1989, *A&A*, 224, 31
- Chini, R., Krügel, E., & Lemke, R. 1996, *A&AS*, 118, 47
- Chini, R., Krügel, E., & Steppe, H. 1992, *A&A*, 255, 87
- Combes, F., Casoli, F., Encrenaz, P., Gerin, M., & Laurent, C. 1991, *A&A*, 248, 607
- Combes, F., Young, L. M., & Bureau M. 2007, *MNRAS*, 377, 1795
- Dahlem, M., Heckman, T. M., Fabbiano, G., Lehnert, M. D., & Gilmore, D. 1996, *ApJ*, 461, 724
- de Vaucouleurs, G., de Vaucouleurs, A., Corwin, H. G., Jr., Buta, R. J., Paturel, G., & Fouque, P. 1991, *Third Reference Catalogue of Bright Galaxies (New York: Springer)*
- Devereux, N., Taniguchi, Y., Sanders, D. B., Nakai, N., & Young, J. S. 1994, *AJ*, 107, 2006
- Downes D. 1989, *Evolution of Galaxies: Astronomical Observations, Lecture Notes in Physics 333*, eds. I. Appenzeller, H. Habing, P. Léna, Springer Verlag, Berlin, p353
- Downes, D., Radford, S. J. E., Guilleoteau, S., Guelin, M., Greve, A., & Morris, D. 1992, *A&A*, 262, 424
- Dumke, M., Nietten, C., Thuma, G., Wielebinski, R., & Walsh, W. 2001, *A&A*, 373, 853
- Elfhag, T., Booth, R. S., Hoeglund, B., Johansson, L. E. B., & Sandqvist, A. 1996, *A&AS*, 115, 439
- Flower, D. R. 2001, *Journal of Physics B Atomic Molecular Physics*, 34, 2731
- Galaz, G., Cortés, P., Bronfman, L., & Rubio, M. 2008, *ApJ*, 677, L13
- Gao, Y., & Solomon, P. M. 1999, *ApJ*, 512, L99
- Gao, Y., & Solomon, P. M., 2004a, *ApJ*, 606, 271
- Gao, Y., & Solomon, P. M., 2004b, *ApJS*, 152, 63.
- Gerin, M., & Phillips, T. G. 2000, *ApJ*, 537, 644
- Golla, G., & Wielebinski, R. 1994, *A&A*, 286, 733
- Graciá-Carpio, J., García-Burillo, S., Planesas, P., & Colina, L. 2006, *ApJ*, 640, L135
- Greve, A., Becker, R., Johansson, L. E. B., & McKeith, C. D. 1996, *A&A*, 312, 391
- Groesbeck, T. D., Phillips, T. G., & Blake, G. A. 1994, *ApJS*, 94, 147
- Güsten, R., Walmsley, C. M., & Pauls, T. 1981, *A&A*, 103, 197
- Hafok, H., & Stutzki, J. 2003, *A&A*, 398, 959
- Handa, T., Nakai, N., Sofue, Y., Hayashi, M., & Fujimoto, M. 1990, *PASJ*, 42, 1
- Hatchell, J., Thompson, M. A., Millar, T. J., & MacDonald, G. H. 1998, *A&AS*, 133, 29
- Heckman, T. M., Blitz, L., Wilson, A. S., Armus, L., & Miley, G. K., 1989, *ApJ*, 342, 735
- Heckman, T. M. 2005, in *Astrophys. Space Sci. Library 329, Starbursts: From 30 Doradus to Lyman Break Galaxies*, eds. R. de Grijs & R. M. González Delgado (Dordrecht: Springer), 3
- Henkel, C., Walmsley, C. M., & Wilson, T. L. 1980, *A&A*, 82, 41
- Henkel, C., & Wiklind, T. 1997, *Space Science Reviews*, 81, 1
- Henkel, C., Wouterloot, J. G. A., & Bally, J. 1986, *A&A*, 155, 193
- Hollenbach, D. J., & Tielens, A. G. G. M. 1997, *ARA&A*, 35, 179
- Huchra, J. 1993, electronic version of “Catalogue of Seyfert Galaxies and Other Bright AGN”
- Iono, D. et al. 2009, *ApJ*, 695, 1537
- Israel, F. P. 2005, *A&A*, 438, 855
- Joint IRAS Science Working Group. 1988. *IRAS Catalogs and Atlases: The Point Source Catalog, Version 2.0 (NASA RP-1190)* (Washington, DC: GPO) (PSC)
- Kaufman, M. J., Wolfire, M. G., Hollenbach, D. J., & Luhman, M. L. 1999, *ApJ*, 527, 795
- Kelly, B. C. 2007, *ApJ*, 665, 1489
- Kenney, J. D. & Young, J. S. 1988, *ApJS*, 66, 261
- Kennicutt, R. C., Jr. 1998, *ARA&A*, 36, 189
- Kennicutt, R. C., Jr., Lee, J. C., Funes, J. G., Sakai, S., & Akiyama, S. 2005, in *Astrophys. Space Sci. Library 329, Starbursts: From 30 Doradus to Lyman Break Galaxies*, ed. R. de Grijs & R. M. González Delgado (Dordrecht: Springer), 187
- Komugi, S., Kohno, K., Tosaki, T., Nakanishi, H., Onodera, S., Egusa, F., & Sofue, Y. 2007, *PASJ*, 59, 55
- Komugi, S., Sofue, Y., Kohno, K., Nakanishi, H., Onodera, S., Egusa, F., & Muraoka K. 2008, *ApJS*, 178, 225
- Kramer, C. et al. 2010, *A&A*, 518, L67
- Kregel, M., & Sancisi, R. 2001, *A&A*, 376, 59
- Krumholz, M. R., & Thompson, T. A. 2007, *ApJ*, 669, 289
- Kuno, N., et al. 2007, *PASJ*, 59, 117
- Leech, J., Isaak, K. G., Papadopoulos, P. P., Gao, Y., & Davis, G. R. 2010, *MNRAS*, 406, 1364
- Lo, K. Y., Hwang, C. Y., Lee, S. W., Kim, D.-C., Wang, W. H., Lee, T. H., Gruendl, R., & Gao, Y. 2000, in *ASP Conf. Ser. 197, Dynamics of Galaxies: from the Early Universe to the Present*, ed. F. Combes, G. A. Mamon & V. Charmandaris (San Francisco, CA:ASP), 279
- Mao, R. Q., Henkel, C., Schulz, A., Zielinsky, M., Mauersberger, R., Störzer, H., Wilson, T. L., & Gensheimer, P. 2000, *A&A*, 358, 433

- Mao, R. Q., Yang, J., Henkel, C., & Jiang, Z. B. 2002, *A&A*, 389, 589
- Matsushita, S., et al. 2004, *ApJ*, 616, L55
- Mauersberger, R., & Henkel, C. 1993, *Rev. M.A.*, 6, 69
- Mauersberger, R., Henkel, C., Walsh, W., & Schulz, A. 1999, *A&A*, 341, 256
- Mei, S., et al. 2007, *ApJ*, 655, 144
- Meier, D. S., Turner, J. L., Crosthwaite, L. P., & Beck, S. C. 2001, *AJ*, 121, 740
- Meier, D. S., Turner, J. L., & Beck, S. C. 2001, *AJ*, 122, 1770
- Moshir, M., Kopman, G., & Conrow, T. A. O. 1992, *IRAS Faint Source Survey, Explanatory Supplement, version 2* (Pasadena, CA: Infrared Processing and Analysis Center, Cal. Tech.)
- Muroaka, K. et al. 2009, *ApJ*, 706, 1213
- Nakanishi, H., Tosaki, T., Kohno, K., Sofue, Y., & Kuno, N. 2007, *PASJ*, 59, 61
- Narayanan, D., Cox, T. J., Shirley, Y., Davé, R., Hernquist, L., & Walker, C. K. 2008, *ApJ*, 684, 996
- Narayanan, D., Groppi, C. E., Kulesa, C. A., & Walker, C. K. 2005, *ApJ*, 630, 269
- Nishiyama, K., & Nakai, N. 2001, *PASJ*, 53, 713
- Oka, T., Nagai, M., Kamegai, K., Tanaka, K., & Kuboi, N. 2007, *PASJ*, 59, 15
- Paturel, G., Petit, C., Prugniel, P., Theureau, G., Rousseau, J., Brouty, M., Dubois, P., & Cambrésy, L. 2003, *A&A*, 412, 45
- Petitpas, G. R., & Wilson, C. D. 2003, *ApJ*, 587, 649
- Petitpas, G. R., & Wilson, C. D. 2004, *ApJ*, 603, 495
- Radford, S. J. E., Downes, D., & Solomon, P. M. 1991, *ApJ*, 368, L15
- Reuter, H. P., Pohl, M., Lesch, H., & Sievers, A. W. 1993, *A&A*, 277, 21
- Reuter, H.-P., Sievers, A. W., Pohl, M., Lesch, H., & Wielebinski, R. 1996, *A&A*, 306, 721
- Sage, L. J., Salzer, J. J., Loose, H.-H., & Henkel, C. 1992, *A&A*, 265, 19
- Salomé, P., et al. 2006, *A&A*, 454, 437
- Sanders, D. B., Mazzarella, J. M., Kim, D.-C., Surace, J. A., & Soifer, B. T. 2003, *AJ*, 126, 1607
- Sanders, D. B., Scoville, N. Z., & Soifer, B. T. 1991, *ApJ*, 370, 158
- Sanders, D. B., Scoville, N. Z., Young, J. S., Soifer, B. T., Schloerb, F. P., Rice, W. L., & Danielson, G. E. 1986, *ApJ*, 305, L45
- Sarzi, M., Allard, E. L., Knapen, J. H., & Mazzuca, L. M. 2007, *MNRAS*, 380, 949
- Sawada, T. et al. 2001, *ApJS*, 136, 189
- Schawinski, K., Thomas, D., Sarzi, M., Maraston, C., Kaviraj, S., Joo, S.-J., Yi, S. K., & Silk, J. 2007, *MNRAS*, 382, 1415
- Schilke, P., Groesbeck, T. D., Blake, G. A., & Phillips, T. G. 1997, *ApJS*, 108, 301
- Schmidt, M. 1959, *ApJ*, 129, 243
- Schulz, A., Henkel, C., Muders, D., Mao, R. Q., Röllig, M., & Mauersberger, R. 2007, *A&A*, 466, 467
- Scoville, N. Z., & Solomon, P. M. 1974, *ApJ*, 187, L67
- Scoville, N. Z., Yun, M. S., & Bryant, P. M. 1997, *ApJ*, 484, 702
- Sil'chenko, O. K., & Afanasiev, V. L. 2002, *A&A*, 385, 1
- Solomon, P. M., Downes, D., & Radford, S. J. E. 1992, *ApJ*, 387, L55
- Solomon, P. M., Downes, D., Radford, S. J. E., & Barrett, J. W. 1997, *ApJ*, 478, 144
- Solomon, P. M., & Vanden Bout, P. A. 2005, *ARA&A*, 43, 677
- Surace, J. A., Sanders, D. B., & Mazzarella, J. M. 2004, *AJ*, 127, 3235
- Sutton, E. C., Jaminet, P. A., Danchi, W. C., & Blake, G. A. 1991, *ApJS*, 77, 255
- Van der Werf, P. et al. 2010, *A&A*, 518, L42
- Véron-Cetty, M. P., & Véron, P. 1991, electronic version of “A Catalog of Quasars and Active Nuclei” (5th ed.; Garching: ESO Sci. Rep. No. 10)
- Vila-Vilaró, B., Cepa, J., & Butner, H. M. 2003, *ApJ*, 594, 232
- Vila-Vilaró, B., Taniguchi, Y., & Nakai, N. 1998, *AJ*, 116, 1553
- Wang, Y., Jaffe, D. T., Graf, U. U., & Evans, N. J., II 1994, *ApJS*, 95, 503
- Warren, B. E. et al. 2010, *ApJ*, 714, 571
- Wiklind, T., Combes, F., & Henkel, C. 1995, *A&A*, 297, 643
- Wiklind, T., & Henkel, C. 1989, *A&A*, 225, 1
- Wilson, C. D., et al. 2008, *ApJS*, 178, 189
- Wilson, C. D., et al. 2009, *ApJ*, 693, 1736
- Yao, L., Seaquist, E. R., Kuno, N., & Dunne, L. 2003, *ApJ*, 588, 771
- Young, J. S., et al. 1995, *ApJS*, 98, 219

TABLE 1 (continued)

No.	SOURCE	R.A. ₂₀₀₀ (^h ^m ^s)	DEC ₂₀₀₀ ([°] ['] ^{''})	v_{hel} (km s ⁻¹)	d_p (Mpc)	D_{25} (['])	i (deg)	M_B (mag)	$\log L_{\text{FIR}}$ (L _⊙)	T_{dust} (K)	Classification		
(1)	(2)	(3)	(4)	(5)	(6)	(7)	(8)	(9)	(10)	(11)	(12)	(13)	(14)
77	NGC 4631	12 42 07.6	+32 32 28	606	8.3	15.5	85	-22.1	10.2	35.9	N	6.6	SB(s)d
78	NGC 4639 ^V	12 42 52.4	+13 15 26	1018	13.9	2.8	52	-19.1	9.0	29.9 ^c		3.5	SAB(rs)bc Sy1.8
79	NGC 4654 ^V	12 43 56.1	+13 07 43	1046	16.5 ^a	5.17	56	-20.5	10.1	31.2	S	5.9	SAB(rs)cd
80	NGC 4666	12 45 08.9	-00 27 38	1520	20.8	4.6	70	-21.0	10.5	33.3	S	4.9	SABc: LINER
81	NGC 4691	12 48 13.4	-03 19 58	1100	15.1	2.52	39	-19.5	9.9	38.4	S	0.4	(R)SB(s)0/a pecHII
82	NGC 4710 ^V	12 49 39.0	+15 09 55	1125	16.5 ^a	4.9	90	-19.7	9.7	33.7	N	-0.8	SA(r)0+? sp HII
83	NGC 4736	12 50 53.5	+41 07 10	308	4.7 ^a	11.2	35	-19.9	9.6	37.4		2.4	(R)SA(r)ab;Sy2 LINER
84	MRK 231	12 54 04.8	+57 08 38	12642	171.7	1.3	53	-22.3	12.3	47.8	U	5.0	SA(rs)c? pec Sy1
85	NGC 4818	12 56 48.8	-08 31 26	1065	14.6	4.3	90	-19.6	10.0	41.3	S	2.0	SAB(rs)ab pec: Sbrst
86	NGC 4826	12 56 44.2	+21 41 05	408	7.5 ^a	10	60	-20.5	9.8	33.8		2.4	(R)SA(rs)ab;HII Sy2
87	NGC 4941	13 04 12.9	-05 33 07	1108	15.1	3.6	36	-19.3	9.0	30.4 ^c		2.4	(R)SAB(r)ab: Sy2
88	NGC 5033	13 13 27.4	+36 35 39	875	12.0	10.7	66	-20.8	9.9	30.2		5.1	SA(s)c Sy1.9
89	NGC 5055	13 15 49.1	+42 02 06	504	10.3 ^a	12.6	56	-21.1	10.2	29.1	S	4.0	SA(rs)bc HII/LINER
90	UGC 8335A ^P	13 15 30.8	+62 07 45	9230	125.6	0.85	L	...	SC; LINER HII
91	UGC 8335B ^P	13 15 35.0	+62 07 29	9313	126.8	1.47	11.6 ^b	44.4 ^b	L	...	SC HII
92	Arp 193 ^P	13 20 35.3	+34 08 25	6985	95.2	1.5	62	-20.5	11.6	40.0	L	9.9	Im: pec;HII LINER
93	NGC 5194	13 29 52.5	+47 11 53	463	7.1 ^a	11.2	30	-20.4	10.1	33.5	S	4.0	SA(s)bc pec;HII Sy2.5
94	M 83	13 37 00.7	-29 51 59	513	4.6 ^a	12.9	46	...	10.2	35.3	S	5.0	SAB(s)c;HII Sbrst
95	NGC 5256 ^P	13 38 17.5	+48 16 37	8353	113.8	1.22	11.4	40.4	L	...	Pec;Sy2;LIRG Sbrst
96	NGC 5257 ^P	13 39 52.9	+00 50 24	6798	92.7	1.8	62	-21.8	11.3 ^b	37.4 ^b	L	3.1	SA(s)b pec;HII LIRG
97	NGC 5258 ^P	13 39 57.7	+00 49 51	6757	92.1	1.7	34	-21.3	11.0 ^b	36.1 ^b	L	3.1	SA(s)b pec;HII LINER
98	NGC 5273	13 42 08.3	+35 39 15	1064	14.6	2.8	57	-18.8	8.8	40.4 ^c		-1.9	SA(s)0 ⁺ 0 ⁺ Sy1.9
99	MRK 273	13 42 51.6	+56 08 13	11326	154.6	0.72	64	-20.8	12.1	47.0	U	...	Ring galaxy;Sy2 LINER
100	NGC 5347	13 53 17.8	+33 29 27	2335	31.9	1.7	45	-19.6	9.6	35.9 ^c		2.0	(R')SB(rs)ab Sy2
101	NGC 5666	14 33 09.5	+10 30 37	2221	30.4	0.95	37	-19.2	9.7	35.9 ^c	S	6.4	S?
102	Arp 302S ^P	14 57 00.3	+24 36 25	10029	136.4	0.6	<11.0 ^b	...	L	...	SC HII
	Arp 302 center	14 57 00.5	+24 36 44	10103	137.4	DBL SYS
103	Arp 302N ^P	14 57 00.7	+24 37 03	10094	137.3	0.9	11.6 ^b	34.0 ^b	L	...	(Sb);HII LINER
104	NGC 5866	15 06 30.2	+55 45 46	672	9.2	4.7	86	-19.9	9.2	29.9		-1.2	S0,3 HII/LINER
105	NGC 5907	15 15 52.9	+56 19 33	667	9.1	12.77	87	-20.9	9.5	27.8	N	5.4	SA(s)c: sp HII:
106	Mrk 848	15 18 05.9	+42 44 53	12049	163.7	0.9	90	-20.4	11.8	44.7	L	-1.7	S0? pec HII
107	NGC 5953	15 34 32.3	+15 11 42	1965	26.9	1.6	44	-19.6	10.3	37.4	S	0.2	SaA: pec;LINER;Sy2
108	Arp 220	15 34 57.2	+23 30 12	5434	74.2	1.5	57	-21.0	12.1	44.7	U	8.4	S?;LINER;HII Sy2
109	NGC 6240	16 52 58.8	+02 24 04	7339	100.0	2.1	82	-21.5	11.7	43.9	L	-0.2	I0: pec;LINER Sy2
110	17208-0014	17 23 22.3	-00 17 02	12834	174.3	0.4	50	-20.2	12.4	44.5	U	3.8	Sbrst HII
111	Arp 293 ^P	16 58 30.6	+58 56 19	5600	76.4	11.2	32.4	L	...	GPair
112	NGC 6524	17 59 14.9	+45 53 17	5698	77.8	1.3	69	-20.9	10.8	34.4 ^c	S	-2.8	S0:
113	NGC 6670B ^P	18 33 34.1	+59 53 21	8428	114.8	-20.1	11.5	38.4	L	-1.1	HII
	NGC 6670 ^P	18 33 35.1	+59 53 21	8650	117.8	1	78	...	11.5	38.4		-1.1	TRP SYS
114	NGC 6670A ^P	18 33 37.7	+59 53 22	8719	118.7	11.5	38.4	L	-1.1	S HII
115	NGC 6814	19 42 40.6	-10 19 24	1563	21.4	3	86	-21.3	10.0	30.5	S	4.0	SAB(rs)bc Sy1.5
116	NGC 6946	20 34 51.9	+60 09 15	48	5.5 ^a	11.5	31	-20.8	9.7	33.7		5.9	SAB(rs)cd;Sy2 HII
117	NGC 7013	21 03 33.1	+29 53 47	779	10.7	4	90	-19.5	8.9	28.9 ^c		0.5	SA(r)0/a LINER
118	NGC 7077	21 29 59.6	+02 24 51	1152	15.8	0.8	79	-16.8	8.5	29.5 ^c	S	-3.9	BCD/E HII
119	NGC 7217	22 07 52.2	+31 21 35	952	13.0	3.9	36	-20.4	9.6	29.3		2.5	(R)SA(r)ab;Sy LINER
120	NGC 7331	22 37 03.5	+34 24 43	816	15.1 ^a	10.5	75	-21.5	10.5	32.7		3.9	SA(s)b LINER
	NGC 7331A	22 37 05.1	+34 24 36	-21.5
121	NGC 7465	23 02 00.8	+15 57 56	1968	26.9	1.2	64	-19.2	10.0	39.3	S	-1.9	(R')SB(s)0 ⁺ 0 ⁺ : Sy2
122	NGC 7469	23 03 15.6	+08 52 26	4892	66.8	1.5	30	-21.7	11.5	41.8	L	1.1	(R')SAB(rs)a Sy1.2
123	NGC 7479	23 04 56.7	+12 19 23	2381	32.6	4.1	36	-21.6	10.6	36.6	S	4.3	SB(s)c;LINER Sy2
124	NGC 7541	23 14 43.7	+04 32 02	2689	31.3 ^a	3.5	75	-21.5	10.7	34.6	S	4.7	SB(rs)bc: pec HII
125	NGC 7679	23 28 46.8	+03 30 41	5138	70.1	1.3	59	-21.2	11.0	39.8	L	-1.3	SB0 pec;HII Sy1 LIRG

The columns contain the following information: Col.(1): The sequence number of the specific source. Col.(2): Galaxy name; ^P: galaxy pair; ^V: Virgo cluster galaxy. Cols.(3) and (4): Right ascension (R.A.) and declination (DEC) in J2000.0 coordinates. Col.(5): Heliocentric velocity (v_{hel}) from NED. Col.(6): Galaxy proper distance calculated from v_{hel} using $H_0 = 73 \text{ km s}^{-1} \text{ Mpc}^{-1}$ and adopting a flat cosmology with $\Omega_M = 0.27$ and $\Omega_\Lambda = 0.73$. ^a: recently measured distances drawn mostly from a crosslink in NED (c.f. NED 1D for references). The distance to Virgo cluster galaxies is set to 16.5 Mpc (Mei et al. 2007). Col.(7): Optical diameter (D_{25}) from NED. Col.(8): Galaxy inclination angle (i) from HyperLEDA. Col.(9): B-band absolute magnitude (M_B) from HyperLEDA. Col.(10): FIR luminosity ($L_{\text{FIR}} = L(40\text{--}400 \mu\text{m})$) calculated following the prescription of Moshir et al. (1992) (see Sec.2.2.1). ^b: calculated with infrared fluxes taken from Surace et al. (2004) where the HIRES processing is adopted allowing for a deconvolution of close galaxy pairs. ^c: sources not included in the RBGS (Sanders et al. 2003); Col.(11): Dust temperature (T_{dust}) derived from the IRAS 60 μm /100 μm color assuming an emissivity that is proportional to the frequency ν . Col.(12): Galaxy classification from this paper; N: normal; S: starburst; L: LIRG; U: ULIRG. All the rest are "pure" AGN (see Sect. 2.2.2). Col.(13): Galaxy type code from HyperLEDA. Col.(14): Galaxy classification from NED.

TABLE 2
GALAXY CLASSIFICATION OF THE SAMPLE

	LINER	Seyfert	Starburst	LIRG	ULIRG
LINER	45	16	20	5	2
Seyfert	16	45	27	8	3
Starburst	20	27	77	24	4
LIRG	5	8	24	24	–
ULIRG	2	3	4	–	4

NOTE. — The diagonal gives the total number of sources of a specific class (e.g., there are 45 LINERS). Nondiagonal coefficients show the number of targets belonging to at least two specific classes (e.g., there are 20 galaxies which have been classified both as LINERS and as starburst galaxies). For details of the classification, see §2.2.2.

TABLE 3 Observed Quantities of the HHT extragalactic CO $J = 3-2$ survey

No.	SOURCE	I_{32} (K km s ⁻¹)	v_{32} (km s ⁻¹)	Δv_{32} (km s ⁻¹)	T_{mb} (mK)	$\log L_{\text{CO}32}$ (K km s ⁻¹ pc ²)	$\log L_{\text{CO}10}$ (K km s ⁻¹ pc ²)	R_{31}	Ref.
(1)	(2)	(3)	(4)	(5)	(6)	(7)	(8)	(9)	(10)
1	IC 10	7.1 ± 0.3	-330 ± 0	14 ± 1	491 ± 30	4.6 ± 0.02	5.1 ± 0.06	0.3 ± 0.05	6 ^{a,†}
2	NGC 157	5.8 ± 0.6*	1733	123	43 ± 10	7.6 ± 0.05	8.2 ± 0.17	0.3 ± 0.10	3 ^a
3	NGC 404	5.5 ± 0.5	-57 ± 2	37 ± 4	140 ± 22	5.8 ± 0.04	6.3	0.4	12 ^a
4	NGC 660	71.1 ± 1.4	843 ± 3	290 ± 6	230 ± 21	8.1 ± 0.01	8.2 ± 0.01	0.7 ± 0.02	3 ^a
5	III ZW 35	4.4 ± 0.6*	8176	141	22 ± 6	8.8 ± 0.07	< 9.4	< 2.0	10 ^c
6	NGC 855	< 2.0	...	(100)	(26)	< 6.4	6	< 2.5	20 ^a
7	NGC 891	17.3 ± 1.0	545 ± 1	59 ± 5	274 ± 40	7.3 ± 0.02	8.1 ± 0.02	0.2 ± 0.01	3 ^{a,†}
8	NGC 972	37.0 ± 0.8	1544 ± 2	225 ± 5	155 ± 13	8.3 ± 0.01	< 8.6	< 2.1	1 ^b
9	MAFFEI 2	157.1 ± 2.3	-23 ± 1	163 ± 3	905 ± 49	7.2 ± 0.01	7.0 ± 0.01	1.6 ± 0.03	8 ^a
10	NGC 1055	19.6 ± 0.9	959 ± 4	175 ± 10	105 ± 18	7.7 ± 0.02	8.0 ± 0.02	0.4 ± 0.03	3 ^a
11	NGC 1068	116.0 ± 1.4	1158 ± 1	228 ± 3	479 ± 24	8.6 ± 0.01	8.8 ± 0.01	0.5 ± 0.02	3 ^a
12	NGC 1084	14.9 ± 0.7	1360 ± 3	144 ± 7	98 ± 14	7.9 ± 0.02	8.2 ± 0.31	0.5 ± 0.34	3 ^a
13	NGC 1087	7.7 ± 0.4	1498 ± 2	82 ± 5	88 ± 11	7.6 ± 0.02	7.9 ± 0.03	0.5 ± 0.04	3 ^a
14	NGC 1275	9.0 ± 0.8	5276 ± 12	248 ± 23	34 ± 14	8.8 ± 0.04	8.5	1.8	22 ^a
15	NGC 1530	30.0 ± 1.1	2417 ± 5	86 ± 9	109 ± 34	8.6 ± 0.05	8.9	0.6	29 ^a
16	NGC 1569	2.9 ± 0.7	-70 ± 5	43 ± 10	64 ± 20	5.2 ± 0.10	5.0 ± 0.04	1.5 ± 0.37	30 ^a
17	NGC 1614	71.1 ± 5.9	4729 ± 9	221 ± 19	303 ± 73	9.6 ± 0.03	9.4 ± 0.01	1.6 ± 0.14	5 ^a
18	NGC 1637	4.9 ± 0.3	729 ± 3	91 ± 6	51 ± 8	7.0 ± 0.03	7.4 ± 0.02	0.4 ± 0.03	3 ^a
19	NGC 2146	66.9 ± 1.5	787 ± 1	124 ± 3	505 ± 36	8.1 ± 0.01	8.4 ± 0.01	0.6 ± 0.02	3 ^{a,†}
20	NGC 2559	37.3 ± 1.6	1497 ± 3	147 ± 8	238 ± 33	8.3 ± 0.02	< 8.9	< 1.2	1 ^b
21	NGC 2655	< 2.6	...	(400)	(17)	< 7.1	< 7.5	< 1.8	1 ^b
22	NGC 2681	17.1 ± 1.7	680 ± 7	137 ± 14	117 ± 40	7.3 ± 0.04	7.5 ± 0.01	0.6 ± 0.06	3 ^a
23	NGC 2768	< 1.5	...	(200)	(14)	< 6.8	6.6	< 1.9	20 ^a
24	Arp 55	11.1 ± 0.7*	11907	305	31 ± 7	9.5 ± 0.03	< 10.0	< 1.6	1 ^b
25	NGC 2782	31.2 ± 2.2*	2587	272	95 ± 25	8.7 ± 0.01	< 8.7	< 1.9	1 ^b
26	NGC 2841	< 4.2	...	(200)	(39)	< 6.5	6.8	< 0.6	3 ^a
27	NGC 2903	59.6 ± 3.4*	525	143	390 ± 69	7.6 ± 0.03	7.8	0.6	8 ^a
28	Arp 303 S	18.6 ± 1.2*	6058	379	42 ± 12	9.2 ± 0.02
29	Arp 303 N	37.8 ± 1.9*	6144	502	62 ± 18	9.5 ± 0.03
30	NGC 2985	8.0 ± 1.3	1226 ± 15	183 ± 38	41 ± 17	7.5 ± 0.07	7.7 ± 0.01	0.7 ± 0.19	3 ^a
31	NGC 3032	4.1 ± 0.8	1535 ± 11	130 ± 31	30 ± 12	7.4 ± 0.08	7.7	0.4	27 ^a
32	NGC 3034	1056.0 ± 6.3	228 ± 1	203 ± 1	4890 ± 166	8.0 ± 0.00	7.9	1.4	8 ^a
33	NGC 3079	93.4 ± 5.5*	1190	408	178 ± 57	8.4 ± 0.03	8.8 ± 0.01	0.4 ± 0.03	25 ^a
34	NGC 3077	8.0 ± 0.3	7 ± 1	42 ± 2	181 ± 12	6.2 ± 0.05	6.0 ± 0.03	1.5 ± 0.10	2 ^a
35	NGC 3110	24.5 ± 0.8	5071 ± 5	325 ± 11	71 ± 8	9.2 ± 0.01	(9.2, 9.8)	(0.5, 1.6)	13 ^{b,d}
36	NGC 3166	< 19.0	...	(300)	(141)	< 7.9	8.2	0.5	12 ^a
37	NGC 3169	11.0 ± 1.1*	1144	259	53 ± 15	7.6 ± 0.05	< 8.3	< 0.4	1 ^b
38	NGC 3147	19.8 ± 1.0	2904 ± 12	466 ± 28	40 ± 8	8.6 ± 0.02	8.5	1.2	29 ^{a,†}
39	NGC 3227	18.1 ± 1.0	1154 ± 7	244 ± 16	70 ± 12	7.8 ± 0.03	8.2 ± 0.03	0.3 ± 0.03	3 ^a
40	HARO 2	2.5 ± 0.3	1452 ± 5	86 ± 9	28 ± 8	7.1 ± 0.05	7.5 ± 0.03	0.4 ± 0.05	21 ^a
41	NGC 3310	6.9 ± 0.7	1032 ± 7	135 ± 13	48 ± 15	7.2 ± 0.04	6.9 ± 0.11	1.9 ± 0.52	3 ^a
42	NGC 3351	26.0 ± 1.4	783 ± 6	200 ± 11	122 ± 27	7.6 ± 0.02	7.4 ± 0.05	1.5 ± 0.19	3 ^a
43	NGC 3367	7.5 ± 1.1	3044 ± 6	86 ± 15	82 ± 22	8.2 ± 0.08	> 8.6	> 0.2	13 ^d
44	NGC 3368	24.6 ± 1.0	885 ± 4	194 ± 10	119 ± 19	7.6 ± 0.02	7.8 ± 0.01	0.7 ± 0.04	3 ^a
45	NGC 3521	14.5 ± 1.4	746 ± 9	178 ± 19	76 ± 20	7.4 ± 0.04	(7.1, 8.2)	<0.6 >0.9	1 ^{b,23d}
46	NGC 3556	14.4 ± 1.8	693 ± 5	94 ± 17	143 ± 31	7.2 ± 0.06	(7.0, 7.9)	(0.9, 1.0)	1 ^{b,31d}
47	NGC 3593	17.3 ± 1.2*	643	128	99 ± 17	7.2 ± 0.02	7.8	0.3	12 ^a
48	NGC 3627	33.4 ± 1.3	717 ± 4	211 ± 9	149 ± 25	7.8 ± 0.02	8.1	0.6	3 ^a
	NGC 3627A	21.9 ± 0.9	673 ± 3	142 ± 8	145 ± 19	7.7 ± 0.02	8	0.5	16 ^a
49	NGC 3628	140.7 ± 1.4	870 ± 1	214 ± 2	618 ± 25	8.4 ± 0.00	8.3 ± 0.02	1.1 ± 0.05	3 ^a
50	NGC 3642	7.4 ± 1.0	1544 ± 19	235 ± 39	29 ± 12	7.6 ± 0.06
51	NGC 3682	12.2 ± 1.6	1584 ± 16	240 ± 35	48 ± 16	7.8 ± 0.06	< 7.6	< 1.7	12 ^e
52	NGC 3690A	36.4 ± 2.4	3155 ± 3	125 ± 12	273 ± 46	8.9 ± 0.03	8.8	1.2	18 ^a
53	NGC 3690B	48.7 ± 1.9	3102 ± 5	239 ± 10	191 ± 33	9.1 ± 0.02	8.9	1.6	18 ^a
54	NGC 3810	20.5 ± 1.6	960 ± 6	145 ± 13	133 ± 24	7.7 ± 0.06	7.5 ± 0.03	1.7 ± 0.18	3 ^a
55	NGC 3982	6.7 ± 0.7	1185 ± 3	61 ± 9	104 ± 16	7.6 ± 0.04	> 7.7	> 0.4	11 ^d
56	IC 750	37.4 ± 2.2	691 ± 6	205 ± 14	172 ± 41	7.6 ± 0.03	7.8 ± 0.03	0.6 ± 0.06	3 ^a
57	NGC 4038	44.0 ± 1.0	1640 ± 1	87 ± 2	473 ± 19	8.4 ± 0.03	8.6 ± 0.06	0.7 ± 0.03	17 ^a
	NGC 4038/9	82.6 ± 2.3*	1515	166	494 ± 25	8.7 ± 0.02	8.8 ± 0.01	0.8 ± 0.02	17 ^a
58	NGC 4039	15.2 ± 1.9*	1657	100	133 ± 30	8.0 ± 0.04	8.5 ± 0.09	0.3 ± 0.04	17 ^a
59	NGC 4102	49.0 ± 3.4*	823	220	172 ± 39	7.9 ± 0.02	8.2	0.6	8 ^a
60	NGC 4138	< 5.3	...	(400)	(34)	< 7.0	< 7.1	< 3.2	1 ^b
61	NGC 4192	7.0 ± 1.4	-191 ± 6	71 ± 19	93 ± 14	7.4 ± 0.09	(7.3, 8.1)	(0.6, 0.8)	14 ^{b,26c}
62	NGC 4254	24.0 ± 1.7*	2434	140	147 ± 20	7.9 ± 0.03	(7.9, 8.4)	(0.5, 1.2)	14 ^{b,23c}
63	NGC 4258	64.4 ± 1.1	407 ± 3	311 ± 6	195 ± 17	7.8 ± 0.01	7.8	0.9	20 ^a
64	NGC 4293	20.4 ± 0.5	933 ± 2	159 ± 4	121 ± 11	7.9 ± 0.01	8.4	0.3	12 ^a
65	NGC 4303	33.7 ± 3.2	1575 ± 6	127 ± 13	250 ± 52	8.1 ± 0.04	(8.1, 8.7)	(0.5, 1.6)	14 ^{b,23c}
66	NGC 4314	37.6 ± 3.0*	1049	187	159 ± 53	7.9 ± 0.03	7.7 ± 0.01	1.6 ± 0.12	3 ^a
67	NGC 4321	56.9 ± 4.2	1590 ± 7	177 ± 14	302 ± 84	8.3 ± 0.03	8.4 ± 0.00	0.7 ± 0.05	3 ^a
68	NGC 4369	8.2 ± 0.6	1035 ± 2	62 ± 5	124 ± 18	7.3 ± 0.03	7.8	0.4	12 ^a
69	NGC 4395	< 2.8	...	(400)	(18)	< 5.8
70	NGC 4414	31.2 ± 0.6	740 ± 3	312 ± 7	94 ± 9	8.3 ± 0.01	8.5 ± 0.03	0.5 ± 0.04	3 ^a
71	NGC 4438	< 11.3	...	(300)	(84)	< 7.6	8.4	< 0.2	3 ^a
72	NGC 4457	20.3 ± 0.7	897 ± 3	168 ± 7	114 ± 14	7.9 ± 0.02	< 8.1	< 2.4	1 ^b
73	NGC 4490	24.4 ± 3.7	669 ± 32	411 ± 68	56 ± 28	7.5 ± 0.07	< 7.3	< 2.1	1 ^b
74	NGC 4527	37.4 ± 5.3*	1642	179	171 ± 48	8.1 ± 0.06	< 8.6	< 1.3	1 ^{b,31d}

TABLE 3 (continued)

No.	SOURCE	I_{32} (K km s ⁻¹)	v_{32} (km s ⁻¹)	Δv_{32} (km s ⁻¹)	T_{mb} (mK)	$\log L_{\text{CO}32}$ (K km s ⁻¹ pc ²)	$\log L_{\text{CO}10}$ (K km s ⁻¹ pc ²)	R_{31}	Ref.
(1)	(2)	(3)	(4)	(5)	(6)	(7)	(8)	(9)	(10)
75	NGC 4565	8.3 ± 1.5	1271 ± 9	91 ± 21	86 ± 28	7.5 ± 0.08	7.6 ± 0.04	0.7 ± 0.14	3 ^a
76	NGC 4594	6.8 ± 0.8	1086 ± 17	292 ± 41	22 ± 8	7.2 ± 0.05	< 7.5	0.9	1 ^b
77	NGC 4631	17.7 ± 0.7	638 ± 1	71 ± 3	233 ± 22	7.2 ± 0.02	7.6	0.4	24 ^a
78	NGC 4639	< 4.5	...	(400)	(29)	< 7.0	< 7.5	...	14 ^b
79	NGC 4654	18.9 ± 1.4	1053 ± 4	95 ± 7	187 ± 40	7.8 ± 0.03	7.9 ± 0.02	0.8 ± 0.07	3 ^a
80	NGC 4666	36.7 ± 3.8	1498 ± 13	242 ± 27	142 ± 45	8.3 ± 0.04	(8.1, 8.8)	(0.8, 1.2)	1 ^b ,31 ^d
81	NGC 4691	12.9 ± 1.0	1129 ± 1	43 ± 4	282 ± 50	7.6 ± 0.03	(7.6, 7.8)	(0.5, 2.7)	1 ^b ,31 ^d
82	NGC 4710	18.7 ± 2.5*	1125	158	90 ± 27	7.8 ± 0.05	(7.8, 8.1)	(0.5, 2.7)	14 ^b ,31 ^d
83	NGC 4736	21.3 ± 2.0*	279	122	133 ± 19	6.8 ± 0.02	7.0 ± 0.04	0.7 ± 0.09	6 ^a ,†
84	MRK 231	8.1 ± 0.8	12690 ± 10	215 ± 24	35 ± 9	9.5 ± 0.04	9.9 ± 0.06	0.4 ± 0.06	6,16 ^a
85	NGC 4818	42.4 ± 1.1	1055 ± 2	123 ± 4	324 ± 26	8.1 ± 0.01	8.1	1	8 ^a
86	NGC 4826	86.8 ± 5.2*	430	214	340 ± 61	7.8 ± 0.02	(7.8, 8.1)	(0.6, 2.0)	1 ^b ,23 ^d
87	NGC 4941	6.7 ± 0.7	1105 ± 3	56 ± 7	113 ± 19	7.3 ± 0.19	> 6.7	> 0.4	11 ^d
88	NGC 5033	16.7 ± 1.1	879 ± 8	240 ± 16	66 ± 13	7.5 ± 0.03	7.6 ± 0.03	0.8 ± 0.08	3 ^a
89	NGC 5055	25.8 ± 3.5*	595	190	99 ± 46	7.5 ± 0.10	8	0.4	8 ^a
90	UGC 8335	3.6 ± 0.6*	9371	154	15 ± 6	8.9 ± 0.05	< 9.6	< 1.2	10 ^c
91	UGC 8335B	8.0 ± 1.2*	9337	106	32 ± 14	9.2 ± 0.08	< 9.7	< 2.7	10 ^c
92	Arp 193	20.5 ± 1.7*	6967	240	64 ± 14	9.4 ± 0.04	9.6 ± 0.09	0.6 ± 0.12	9 ^a
93	NGC 5194	44.4 ± 2.8	422 ± 2	61 ± 5	681 ± 87	7.5 ± 0.03	7.5 ± 0.05	1.0 ± 0.13	6 ^a ,†
94	M 83	153.9 ± 3.1	519 ± 1	112 ± 3	1290 ± 76	7.6 ± 0.01	7.6	1.1 ± 0.06	28 ^a
95	NGC 5256	5.7 ± 0.9*	8369	278	18 ± 5	9.0 ± 0.05	< 9.8	< 1.2	10 ^c
96	NGC 5257	18.2 ± 1.5	6787 ± 13	312 ± 29	55 ± 16	9.3 ± 0.04	> 9.3	> 0.5	13 ^d
97	NGC 5258	27.0 ± 1.1	6806 ± 8	347 ± 16	73 ± 12	9.5 ± 0.02	> 9.3	> 0.7	13 ^d
98	NGC 5273	< 0.9	...	(100)	(11)	< 6.4	> 6.4	...	11 ^d
99	MRK 273	20.1 ± 0.7*	11355	471	35 ± 6	9.8 ± 0.02	9.8 ± 0.02	0.9 ± 0.05	5 ^a
100	NGC 5347	12.0 ± 1.4	2382 ± 4	78 ± 10	144 ± 28	8.2 ± 0.08	(7.7, 8.5)	(1.7, 3.9)	7 ^c ,11 ^d
101	NGC 5666	9.2 ± 1.8	2321 ± 29	276 ± 51	31 ± 17	8.0 ± 0.08	8.2 ± 0.02	0.7 ± 0.15	20 ^a
102	Arp 302S	8.5 ± 1.5*	9774	232	27 ± 11	9.3 ± 0.07	< 9.6	< 3.4	10 ^c
	Arp 302 center	< 4.9	...	(400)	(22)	< 9.0
103	Arp 302N	18.1 ± 1.1*	10281	548	21 ± 9	9.6 ± 0.07	< 10.4	< 1.3	10 ^c
104	NGC 5866	< 8.6	...	(200)	(78)	< 7.0	7.2	< 0.6	12 ^a
105	NGC 5907	8.4 ± 0.7	663 ± 3	82 ± 9	96 ± 19	7.0 ± 0.04	7.5 ± 0.02	0.3 ± 0.03	3 ^a
106	Mrk 848	4.2 ± 0.4	12111 ± 4	88 ± 11	44 ± 7	9.1 ± 0.05	9.4	0.5	19 ^a
107	NGC 5953	21.5 ± 2.2*	2003	147	112 ± 40	8.3 ± 0.04	(8.4, 8.6)	(0.5, 2.3)	13 ^d
108	Arp 220	58.5 ± 1.9*	5427	379	129 ± 8	9.6 ± 0.02	9.9 ± 0.04	0.5 ± 0.05	7,15 ^a
109	NGC 6240	74.9 ± 2.2*	7394	355	186 ± 21	10.0 ± 0.01	9.9 ± 0.09	1.1 ± 0.22	15,4 ^a
110	17208-0014	24.6 ± 1.4	12857 ± 11	386 ± 24	60 ± 9	10.0 ± 0.03	9.9 ± 0.09	1.2 ± 0.26	15 ^a
111	Arp 293	13.3 ± 1.8*	5431	282	56 ± 14	9.0 ± 0.05	< 9.5	< 1.4	1 ^b
112	NGC 6524	6.6 ± 1.1	5659 ± 10	125 ± 24	49 ± 14	8.7 ± 0.07
113	NGC 6670B	19.8 ± 1.8*	8618	360	58 ± 20	9.5 ± 0.07	< 9.9	< 2.8	10 ^c
	NGC 6670	8.3 ± 0.7*	8688	268	45 ± 19	9.2 ± 0.04	< 10.2	< 0.7	10 ^c
114	NGC 6670A	16.2 ± 1.5*	8702	307	27 ± 8	9.5 ± 0.05	< 9.8	< 3.5 ^a	10 ^c
115	NGC 6814	2.1 ± 0.2	1557 ± 7	119 ± 13	17 ± 4	7.1 ± 0.06	(7.3, 8.1)	(0.3, 0.5)	1 ^b ,11 ^d
116	NGC 6946	132.3 ± 1.8	60 ± 1	150 ± 2	827 ± 56	7.7 ± 0.01	7.8 ± 0.03	0.9 ± 0.07	6 ^a
117	NGC 7013	10.5 ± 0.8	829 ± 13	352 ± 30	28 ± 7	7.2 ± 0.03	7	1.4	12 ^a
118	NGC 7077	0.8 ± 0.2	1015 ± 16	222 ± 31	19 ± 7	6.4 ± 0.06	6.3	1.1 ± 0.38	21 ^a
119	NGC 7217	8.1 ± 0.7	924 ± 12	269 ± 25	28 ± 8	7.2 ± 0.04	7.3 ± 0.02	0.8 ± 0.08	3 ^a
120	NGC 7331	7.2 ± 0.6*	884	50	74 ± 15	7.3 ± 0.03	8.0 ± 0.01	0.2 ± 0.02	3 ^a
	NGC 7331A	12.6 ± 1.0*	903	145	86 ± 25	7.6 ± 0.05	8.0 ± 0.01	0.3 ± 0.03	3 ^a
121	NGC 7465	6.3 ± 0.9	1970 ± 10	127 ± 17	47 ± 16	7.8 ± 0.06	< 8.2	< 1.6	1 ^b
122	NGC 7469	35.2 ± 1.3	4949 ± 5	249 ± 10	133 ± 22	9.3 ± 0.02	(8.8, 9.4)	(1.5, 3.4)	1 ^b ,11 ^d
123	NGC 7479	20.1 ± 1.3	2381 ± 8	238 ± 19	79 ± 15	8.4 ± 0.03	< 9.1	< 1.6	1 ^b
124	NGC 7541	17.8 ± 0.9	2673 ± 4	144 ± 9	116 ± 20	8.3 ± 0.02	8.5	0.6	8 ^a ,†
125	NGC 7679	17.2 ± 1.4*	5110	285	55 ± 29	9.0 ± 0.05	< 9.0	(1.1, 2.4)	12 ^e

The columns contain the following information: Col.(1): Sequence number. Col.(2): Galaxy name. Cols.(3)–(6): The CO(3–2) line intensity ($I_{32} = \int T_{\text{mb}} dv$), LSR velocity, width (FWHM), and main beam brightness temperature, respectively, with corresponding standard errors from Gaussian fits or from *moments in the case of non-Gaussian line shapes. Non-detections are listed with their rms noise level σ (Col.(6) values in brackets) at a channel spacing of $\delta v \sim 6.6 \text{ km s}^{-1}$. In these cases the full width of the CO(1–0) line (ΔV_{10} , Col.(5) values in brackets) was estimated from spectra taken from the literature or was set to 400 km s^{-1} ; corresponding upper limits for I_{32} were obtained using $I_{32} < 3\sigma \times (\Delta V_{10} \times \delta v)^{1/2}$ (Col.(3)). Col.(7): The CO(3–2) luminosity calculated with Eq.(1) (see § 4.1) for a beam of $\Theta_{\text{mb}} = 22''$. Col.(8): The CO(1–0) luminosity calculated with an equation similar to that of $L_{\text{CO}(3-2)}$ for galaxies with IRAM-30m CO(1–0) data available in the literature (listed in Col.(10)); otherwise either upper or lower limits are given, depending on the telescope used for CO(1–0). Col.(9): The CO(3–2)/CO(1–0) line intensity ratio R_{31} and its standard deviation for galaxies with IRAM-30m CO(1–0) data available in the literature (listed in Col.(10)); otherwise either upper or lower limits are given, depending on the telescope used for the CO(1–0) data. Col.(10): References for the CO(1–0) data: 1. Young et al. (1995); 2. Albrecht et al. (2004); 3. Braine et al. (1993); 4. Combes et al. (1991); 5. Gao & Solomon (2004b); 6. Gerin et al. (2000); 7. Heckman et al. (1989); 8. Mauersberger et al. (1999); 9. Radford et al. (1991); 10. Sanders et al. (1991); 11. Vila-Vilaró et al. (1998); 12. Wiklind & Henkel (1989); 13. Yao et al. (2003); 14. Kenney et al. (1988); 15. Solomon et al. (1997); 16. Reuter et al. (1996); 17. Schulz et al. (2007); 18. Casoli et al. (1989); 19. Chini et al. (1992); 20. Wiklind et al. (1995); 21. Sage et al. (1992); 22. Reuter et al. (1993); 23. Nishiyama et al. (2001); 24. Golla & Wielebinski (1993); 25. Handa et al. (1990); 26. Kuno et al. (2007); 27. Combes et al. (2007); 28. Baan et al. (2008); 29. Solomon et al. (1992); 30. Greve et al. (1996); 31. Komugi et al. (2008). Telescopes used are ^a IRAM-30m; ^b FCRAO-14m; ^c NRAO-12m; ^d NRO-45m; ^e OSO-20m. †: The CO(1–0) data was taken at an offset position $> 5''$ relative to our CO(3–2) position.

TABLE 4
 $^{12}\text{CO}(3-2)/(1-0)$ INTEGRATED LINE INTENSITY RATIOS.

galaxy type	R_{31} statistics					
	N	mean ^d	σ^e	median	min	max
(activity)						
normal	7	0.61 ± 0.16	0.42	0.44	0.26	1.51
LINER ^a	20	0.65 ± 0.08	0.36	0.57	0.19	1.57
Seyfert ^a	12	0.82 ± 0.12	0.43	0.75	0.27	1.79
‘pure’ AGN ^b	18	0.78 ± 0.09	0.37	0.70	0.19	1.57
starburst ^c	25	0.89 ± 0.11	0.53	0.71	0.25	1.93
(U)LIRG	10	0.96 ± 0.14	0.45	0.99	0.37	1.63
(bar)						
SA	18	0.62 ± 0.10	0.41	0.50	0.19	1.71
SAB	16	0.80 ± 0.11	0.44	0.72	0.25	1.93
SB	12	0.88 ± 0.15	0.53	0.67	0.30	1.63
Total	61	0.81 ± 0.06	0.46	0.69	0.19	1.93

^a Including starbursts but not (U)LIRG overlaps.

^b See §. 2.2.2 for details.

^c Excluding (U)LIRGs.

^d The mean value and its standard error.

^e Standard deviation of an individual target.

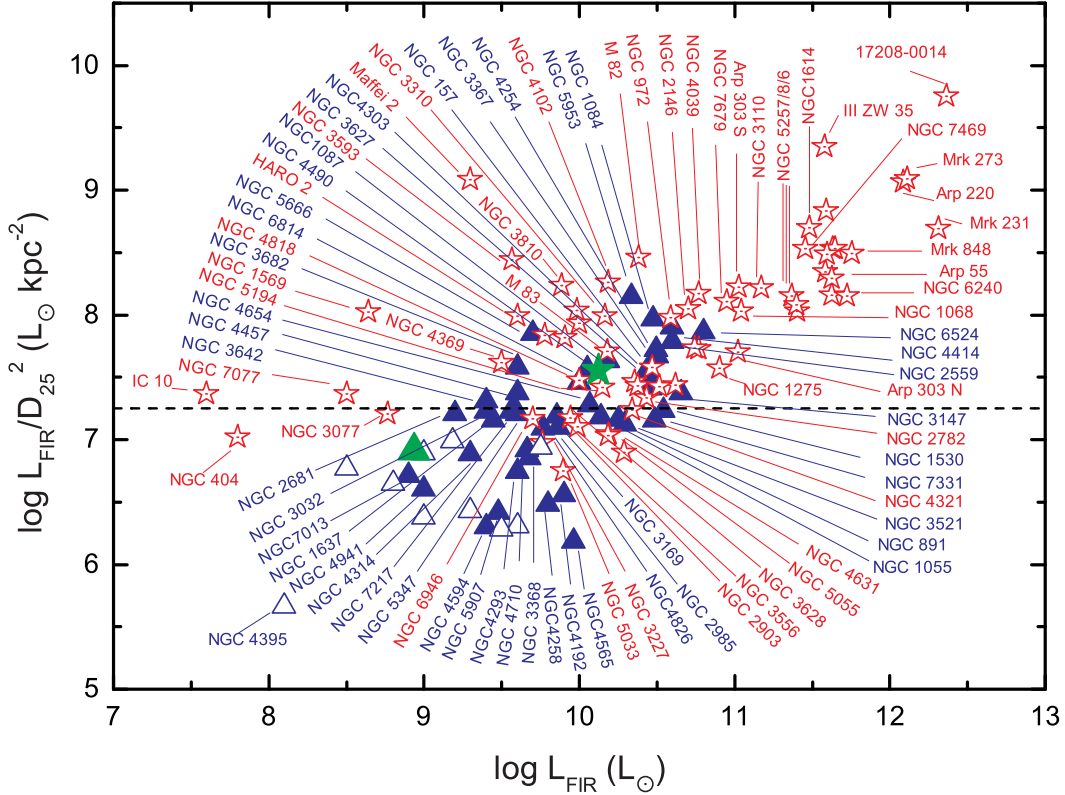


FIG. 1.— Starburst definition: Red open stars denote galaxies classified as starbursts in the literature. Blue triangles mark galaxies not being classified as such. All our CO $J = 3-2$ non-detections arise from the latter sample and are marked by open triangles. Also marked are NGC 253 (by a green star), a typical starburst galaxy (e.g., Brunthaler et al. 2009), and IC 342 (by a green triangle), a galaxy similar to the Milky Way (Downes et al. 1992). The dashed horizontal line, with $\log(L_{\text{FIR}}/D_{25}^2) = 7.25 \text{ L}_{\odot} \text{ kpc}^{-2}$, is used as the borderline between starburst and non-starburst galaxies throughout this paper.

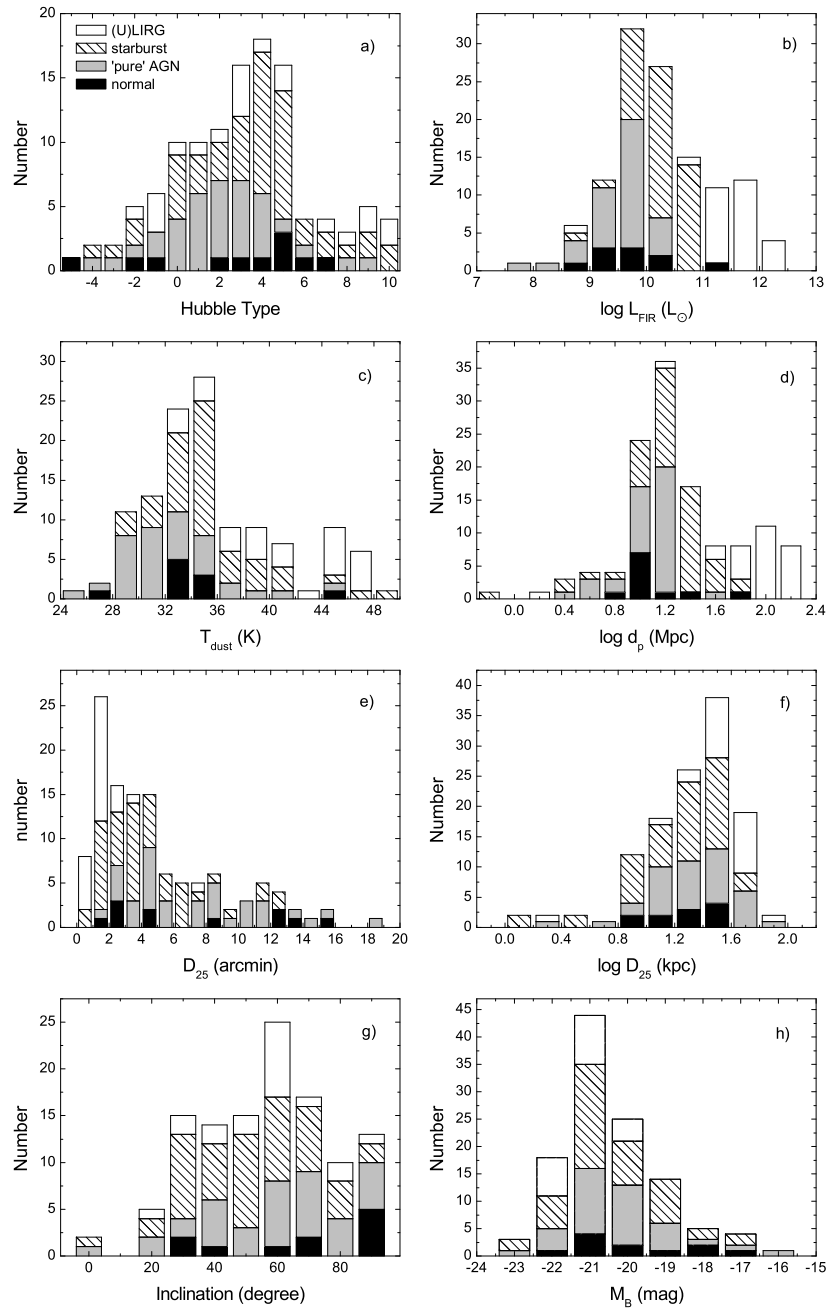


FIG. 2.— Number distributions of the observed galaxy sample: a) Hubble type (see de Vaucouleurs et al. 1991), b) far-infrared luminosity, c) $60\mu\text{m}/100\mu\text{m}$ dust color temperature, d) distance, e) optical angular size, f) linear size, g) inclination, and h) B-band magnitude of the observed sample.

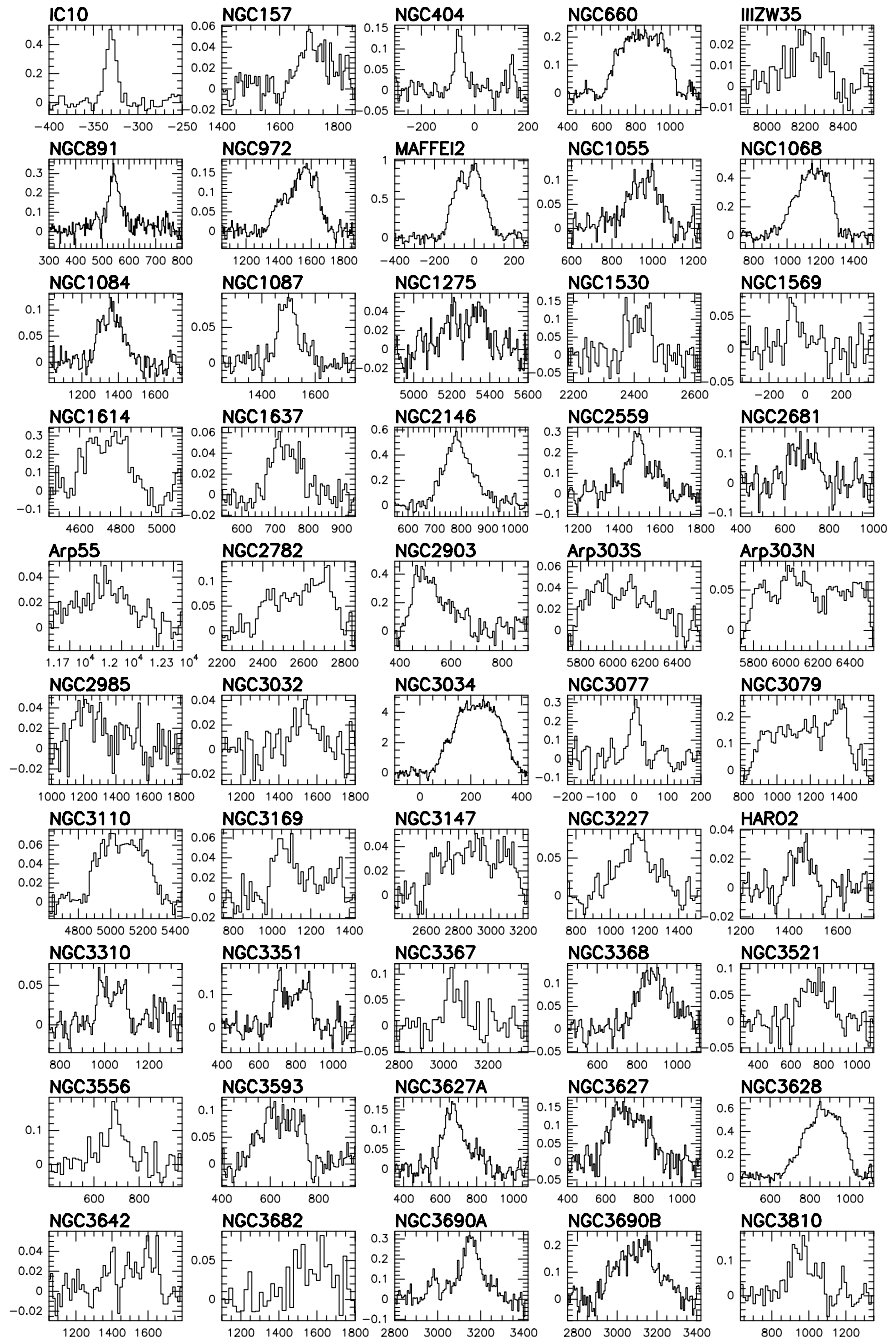


FIG. 3.— CO $J = 3-2$ spectra. The velocity scale corresponds to Local Standard of Rest in units of km s^{-1} . The intensity is displayed in units of main beam brightness temperature (K).

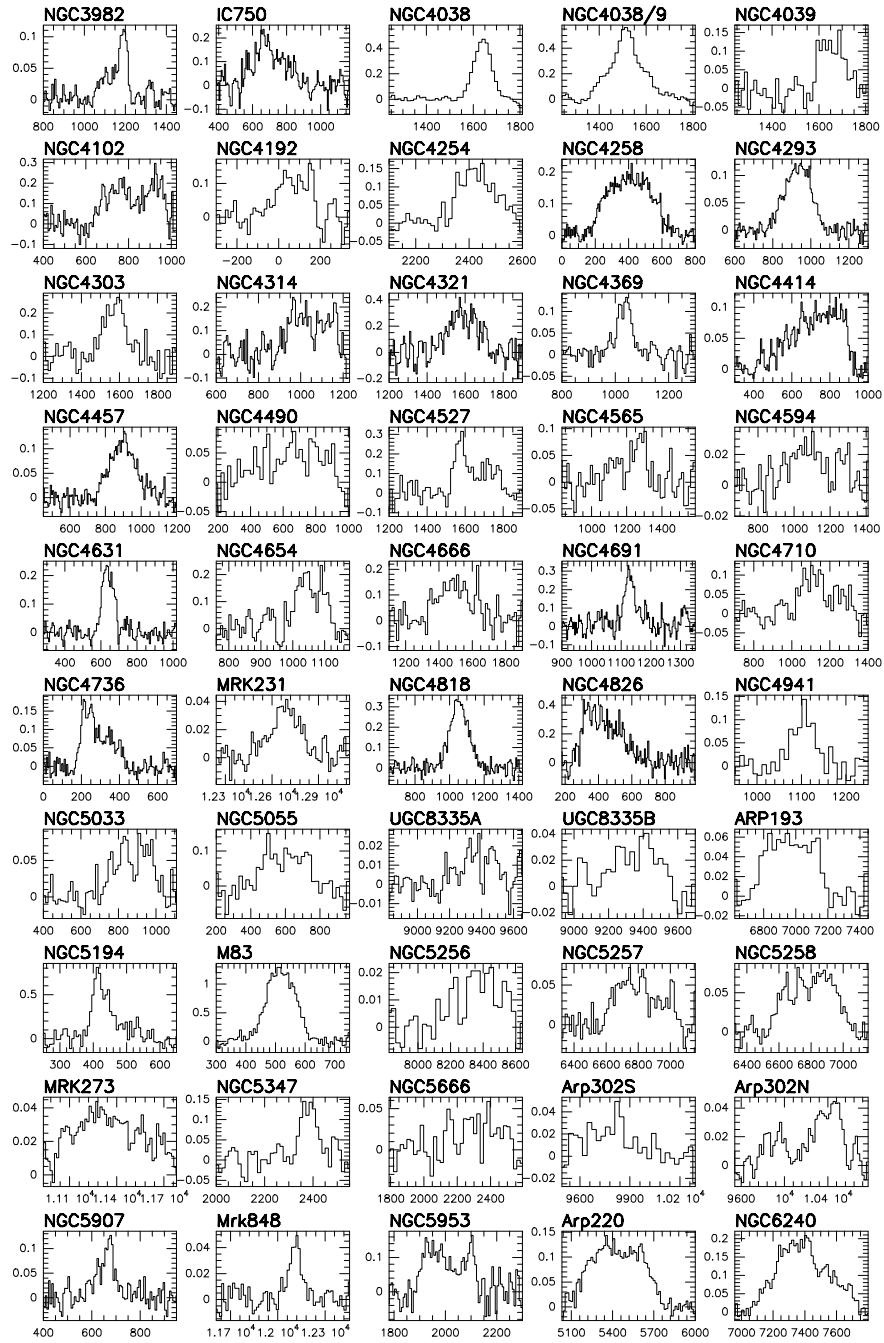


FIG. 3.— (Continued)

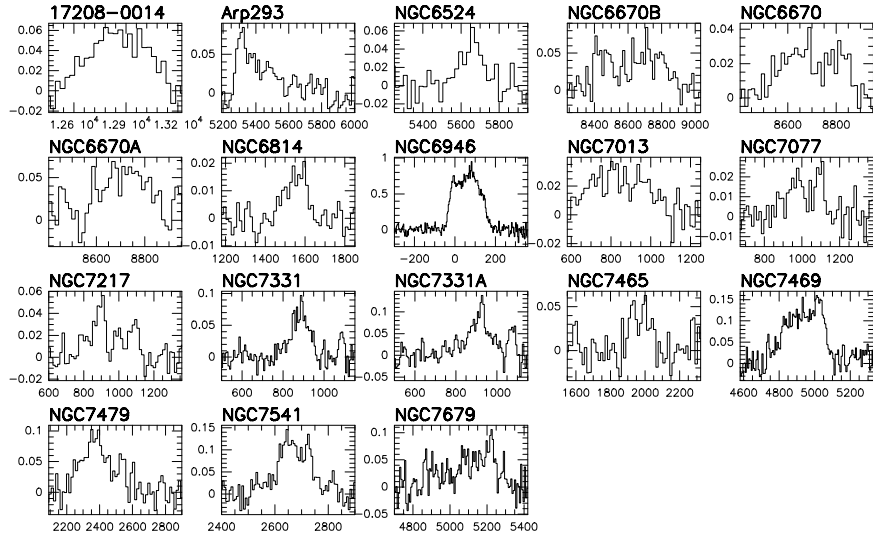


FIG. 3.— (Continued)

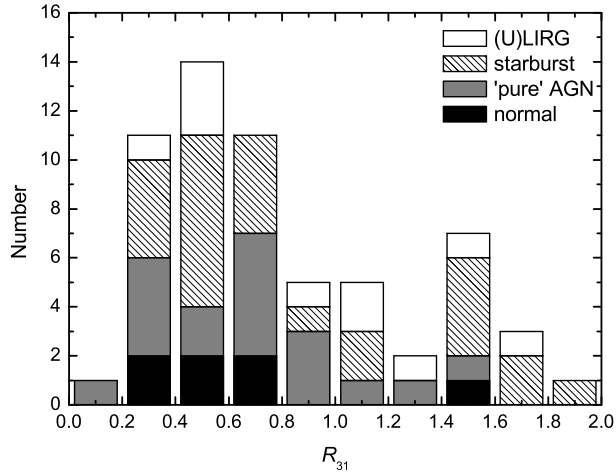


FIG. 4.— Number distribution of the matching beam line intensity ratio R_{31} for 61 galaxies from our sample (see § 5.1.2 for details).

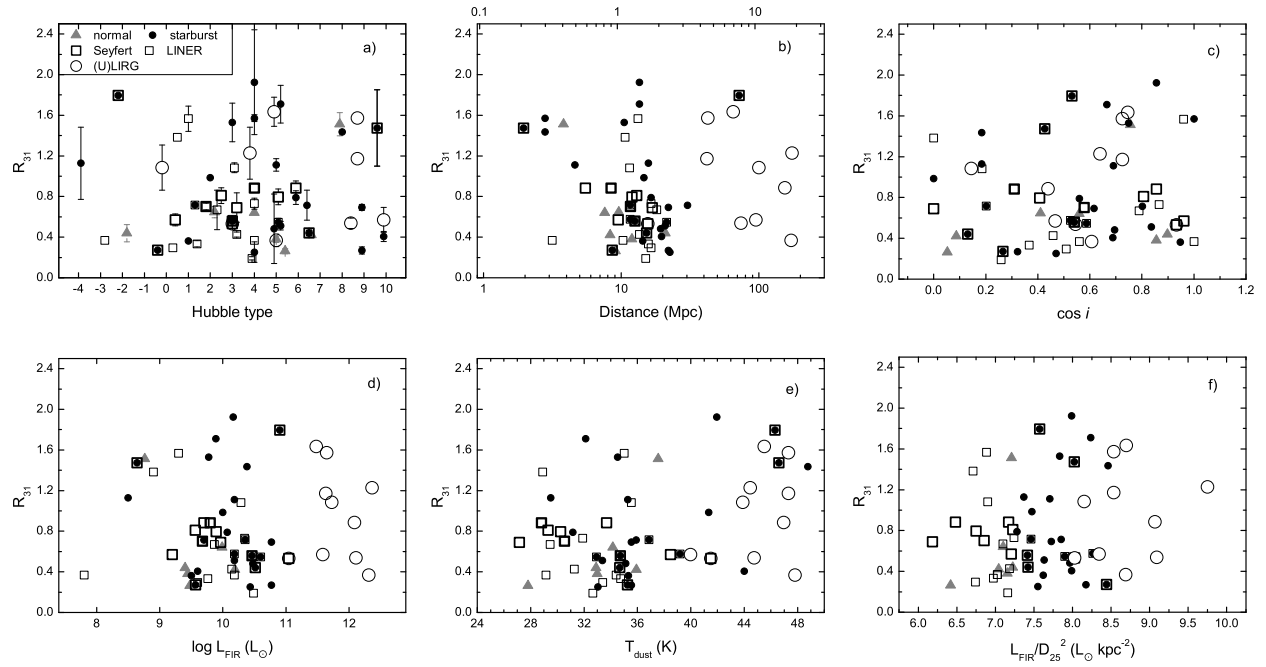


FIG. 5.— R_{31} versus a) Hubble type, b) distance (the lower X-axis) or projected beam size (the upper X-axis in kpc) c) cosine of the inclination, d) FIR luminosity, e) dust temperature, and f) FIR luminosity per unit area (L_{FIR}/D_{25}^2) of sample galaxies with galaxy types being indicated in a). The error bars are removed for clarity in the panels b) – f).

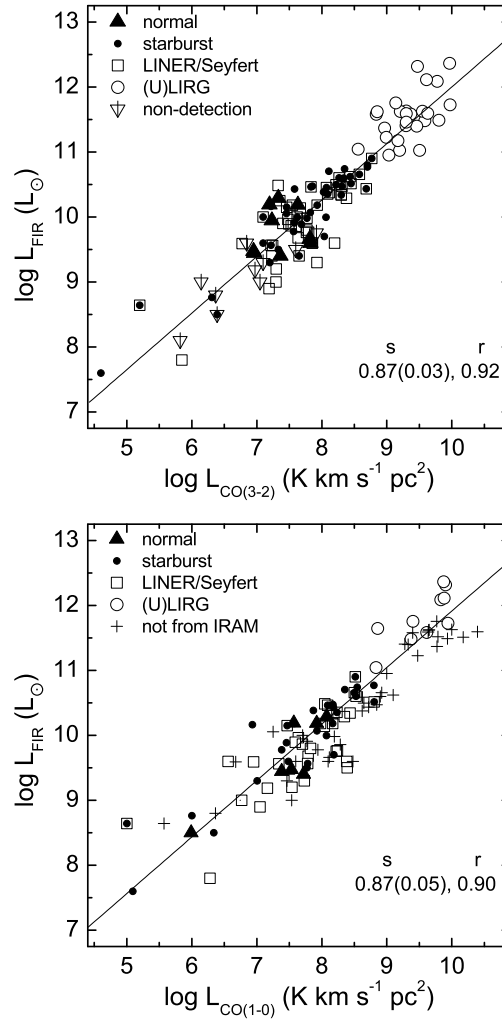


FIG. 6.— Log-log plot of the correlation between nuclear CO and global FIR luminosity for CO(3–2) (upper panel) and CO(1–0) (lower panel). Both CO line luminosities cover the central $22''$ region, except for the crosses representing CO(1–0) data with the larger ($\sim 50''$) beams of the FCRAO-14m or NRAO-12m telescopes. Straight lines show linear regression fits to the unweighted data. Slopes (s) and correlation coefficients (r) are given at the lower right corner of each panel. Only our CO(3–2) detections and CO(1–0) data from the IRAM-30m are included in the fits. Non-detections (upper limits) and data from the FCRAO and NRAO were not considered. IC 10, the isolated dot at the lower left corner of each panel, is also not part of the fits (see § 5.2.2).

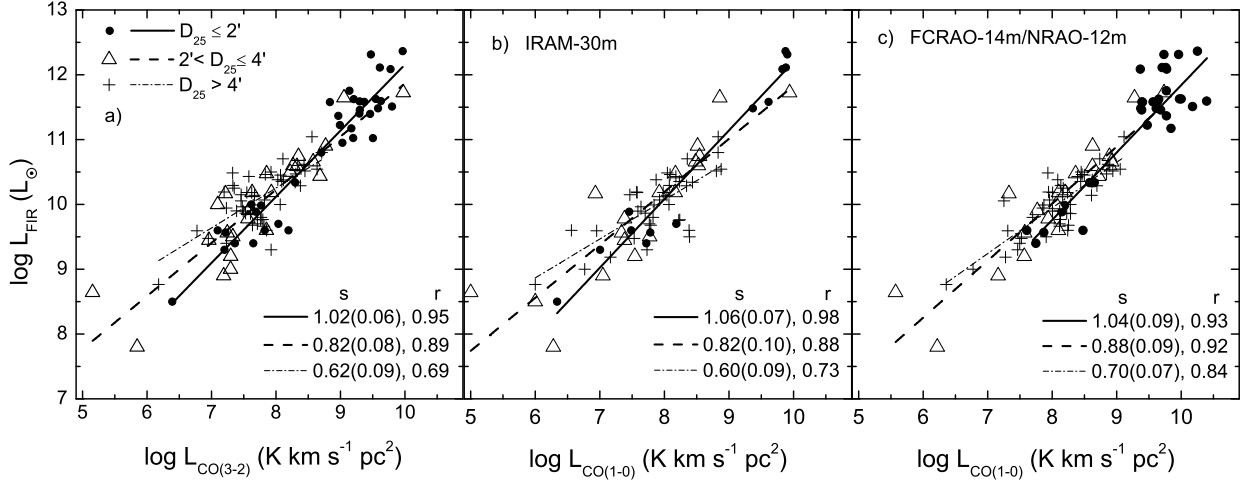


FIG. 7.— Log-log correlation of a) $L_{\text{CO}(3-2)}$ and L_{FIR} (this work), b) $L_{\text{CO}(1-0)}$ and L_{FIR} (CO from the IRAM-30m telescope), and c) $L_{\text{CO}(1-0)}$ and L_{FIR} (CO from the FCRAO-14m and NRAO-12m antennas), with our sample galaxies being divided into three groups characterized by their optical angular sizes (D_{25}): 1) $D_{25} \leq 2'$ (filled circles, solid lines denoting the corresponding linear regression fit), 2) $2' < D_{25} \leq 4'$ (empty triangles, dashed lines), and 3) $4' < D_{25} \leq 18'$ (crosses, dash-dotted lines). The corresponding slopes (s) and correlation coefficients (r) are also given.

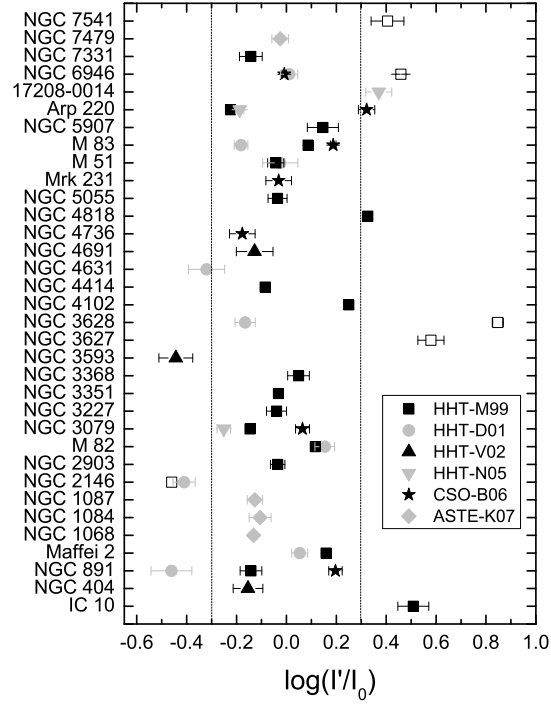


FIG. 8.— A comparison of our integrated CO(3–2) intensities with previously published results. The horizontal axis gives the logarithmic intensity deviation, where I' denotes the integrated CO(3–2) intensity taken from the literature, while I_0 is from this work. Data points measured at nominal position offsets $\gtrsim 5''$ are represented as open squares. A pair of vertical lines marks the ± 0.3 dex deviation limits. For the references given in the lower right box, see §A.1.

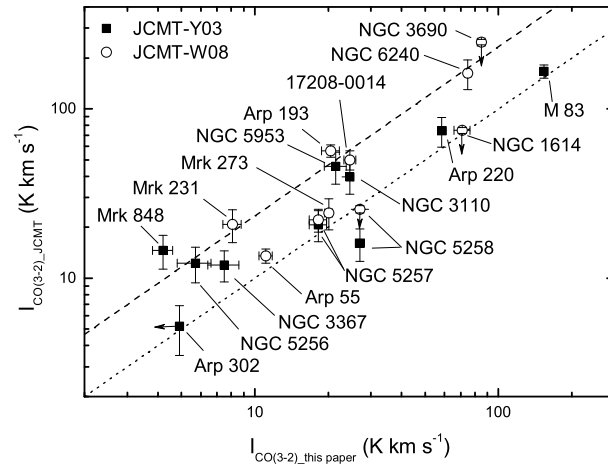


FIG. 9.— A comparison of CO(3–2) integrated intensities for galaxies observed with the JCMT–15m (by Yao et al. (2003, JCMT-Y03) and Wilson et al. (2008, JCMT-W08)) and with the HHT–10m in this paper. Two straight lines denote the theoretical relationship of intensities obtained with the two telescopes assuming point-like (dashed) and uniformly-extended (dotted) structures with respect to the observing beams.